Key Points:
- New models of sedimentary basins and depth to the Moho of South America were developed to improve lithospheric modeling
- Deep depleted roots under the Amazon, Paranapanema, and São Francisco cratons are evident from models of lithospheric temperatures, densities, and composition
- Depletion south of the Paranapanema Craton indicates a previously larger extent of the craton

Supporting Information:
Supporting Information may be found in the online version of this article.

Correspondence to:
N.-P. Finger,
finger@gfz-potsdam.de

A Thermo-Compositional Model of the Cratonic Lithosphere of South America

N.-P. Finger[1,2] , **M. K. Kaban[1,3]** , **M. Tesauro[4,5]** , **C. Haeger[1]** , **W. D. Mooney[6]** , and **M. Thomas[1,2]**

[1]German Research Centre for Geosciences, Potsdam, Germany, [2]FU Berlin, Berlin, Germany, [3]Schmidt Institute of Physics of the Earth, Moscow, Russia, [4]University of Trieste, Trieste, Italy, [5]University of Utrecht, Utrecht, The Netherlands, [6]US Geological Survey, Menlo Park, CA, USA

Abstract New seismic data on the crust and upper mantle of South America have recently become available and describe its deep structure with unprecedented resolution. Here, seismic data are combined with gravity data and mineral physics constraints to develop self-consistent models of the temperature, composition, and density of the South American lithospheric and sub-lithospheric upper mantle. A new model of the crustal structure was developed, including sediment and average crustal density and depth to the Moho. This crustal model was used to correct the gravity field and obtain the residual topography. Then, an initial temperature model, derived from seismic tomography and mineral physics, was improved through an iterative process based on the joint inversion of gravity and residual topography. The results reveal deep cratonic roots present under wide parts of the Amazon, São Francisco, and Paranapanema Cratons, but not under the Rio de la Plata and Parnaíba Cratons. These cratons probably never developed lithospheric roots or were rejuvenated during subsequent tectonic events. We hypothesize that the root of the northwestern Amazon craton was removed by upwelling of hot mantle material under the Guyana highlands. Temperature and density anomalies evident beneath the São Francisco Craton appear to be connected with those of the Paranapanema Craton, which could indicate a westward shift of its root. Depletion south of the Paranapanema Craton probably denotes remnants of a previously larger craton that was rejuvenated by the upwelling of hot mantle material leading to emplacement of the Paraná Flood Basalts.

Plain Language Summary The lithosphere and upper mantle of South America is investigated using multiple data sets, including the topography, crustal structure, regional seismic tomography, gravity, and mineral physics. These data are jointly inverted to estimate variations in temperature, density and composition in the lithospheric and sub-lithospheric upper mantle to a depth of 325 km. Our results show significant variations in lithospheric properties, including thick, depleted roots beneath large parts of the Amazon, São Francisco, and Paranapanema Cratons. However, portions of some cratons, such as the western Guyana Shield, lack a depleted root. We hypothesize that these regions either never developed a depleted root, or that the root was rejuvenated by lithospheric processes.

1. Introduction

Tectonic processes, which shape the surface of the Earth and cause its seismic activity, are driven by strong heterogeneities of density and temperature in the mantle that are not visible at the surface. While temperature variations govern mantle viscosity, density also depends on mantle composition, among other factors. A special role is played by cratons, the stable, Archean to Proterozoic parts of the continents. Cratons are usually underlain by cold, thick, and seismically fast lithosphere (Schaeffer & Lebedev, 2015). Although density increases with decreasing temperature, cratons are often neutrally or even positively buoyant. This is caused by iron depletion due to partial melting and melt fractionation over time (Jordan, 1978). Seismic velocities are less sensitive to these compositional density variations than the gravity field, which in turn does not allow robust estimations of temperature. Therefore, multiple methods hold the potential to construct a more comprehensive model of the lithosphere and upper mantle. In this study, we combine gravity and seismic data, constrained by mineral physics, to model the lithospheric and sub-lithospheric upper mantle of South America using an approach that has been applied to other continents (e.g., Kaban et al., 2014; Tesauro et al., 2014a).
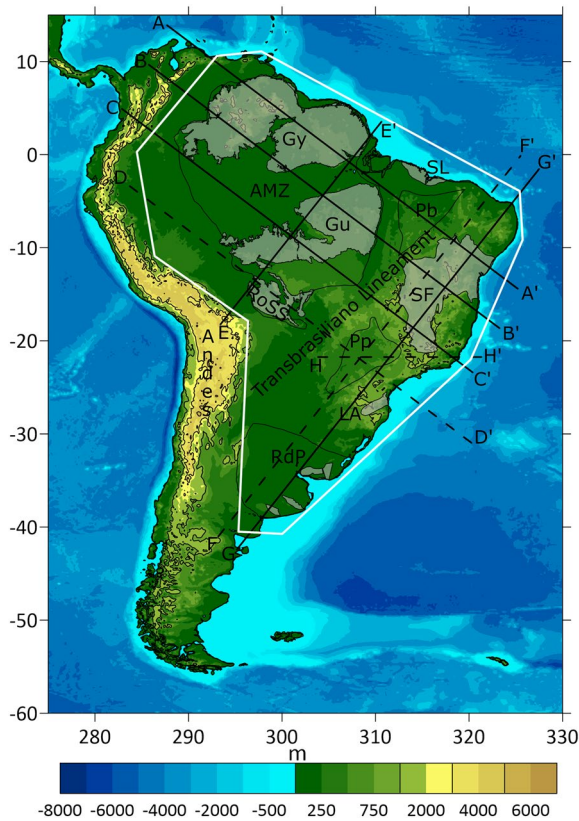
Figure 1. Bathymetry and topography of South America and surrounding regions. Black outlines denote (proposed) cratons. Cratonic shields and outcrops are shaded in light gray. White outline marks the area of interest for this study. Profiles shown in the discussion are marked by thick black lines, profiles marked with dashed lines can be found in the supporting information. Gy and Gu, Guyana and Guaporé Shields; RoSS, Rondonia-San Ignácio and Sunsás Province; AMZ, Amazon Craton (Rizzotto & Hartmann, 2012), non-shield area covered by the Solimões (west) and Amazon (east) Basins; SL, São Luis Craton; Pb, Parnaíba Craton, covered by the basin of the same name; SF, São Francisco Craton; Pp, Paranapanema Craton, covered by sediments of the Paraná Basin; LA, Luiz Alves Craton (Cordani et al., 2016); RdP, Rio de la Plata Craton (Oyhantçabal et al., 2011; Sanchez Bettucci et al., 2010).

The present study focuses on the South American Platform, the stable part of the South American continent that is comprised of several cratons and cratonic fragments. These have been the target of geoscientific studies over the past decades, but some of these results are still under debate. For example, outcrops of the Rio de la Plata Craton are limited to coastal areas, but the subsurface extent of this craton is proposed to reach as far as the Andean forelands (e.g., Oyhantçabal et al., 2011; Santos et al., 2019). The Paranapanema Craton is proposed to be covered by sediments of the Paraná Basin (Mantovani et al., 2005), a hypothesis that is debated (e.g., Bologna et al., 2019; Chaves et al., 2016; Dragone et al., 2017). Another cratonic fragment is inferred to underlie the Parnaíba Basin from gravity data analysis (de Castro et al., 2014). While those studies mostly target the crustal part of the lithosphere using a variety of geophysical methods, knowledge of the state and structure of the lithospheric mantle is mainly inferred from regional (e.g., Celli et al., 2020; Chulick et al., 2013; Heintz et al., 2005) or global seismic tomography (e.g., Schaeffer & Lebedev, 2015; Steinberger & Becker, 2018). Therefore, separating the opposing density effects of cooling versus iron depletion through the application of integrated geophysical models can further improve understanding of the cratonic lithosphere and its role in mantle dynamics and continental evolution. To reach this goal, the approach of Kaban et al. (2014) and Tesauro et al. (2014a) was applied using a combined analysis of the gravity data available in model Eigen-6C4 (Förste et al., 2014), data on the crustal structure (e.g., Rivadeneyra-Vera et al., 2019) and the new S-wave tomography SA2019 (Celli et al., 2020) at a scale of $1° \times 1°$.

1.1. Geologic Setting

The South American continent can be divided into three major parts. The youngest part consists of two Phanerozoic mountain belts at the western (Andes) and northern (Caribbean) borders of the continent. They originate from the collision zones with adjacent Cocos, Nazca (Andes), and Caribbean tectonic plates and make up the tectonically active regions of the continent. The second and largest part, the South American Platform (Cordani et al., 2000), spreads from the Andean forelands to the Atlantic Ocean and from the Caribbean Sea to the Chaco-Paraná Basin in northern Argentina (Figure 1). It consists of the Archean to Proterozoic Amazon Craton in the north and São Francisco Craton in the east as well as several minor cratons and cratonic fragments.

The large Amazon Craton is divided in several zones of different age, of which the older ones (>2 Ga) lie to the east and progressively younger terrains are located to the west and south with the 1 Ga Rondonia-San Ignácio and Sunsás Provinces (RoSS) at the southwestern edge of the craton (Teixeira et al., 1989). A SW-NE trending network of fold belts and tectonic provinces was created during the Neoproterozoic formation of the Gondwana supercontinent that separates the Amazon Craton from the other cratonic blocks to the East and South (de Brito Neves & Cordani, 1991). A major feature of this network is the Trans-Brasiliano Lineament (TBL) that probably resulted from the collision of the Amazon and São Francisco-Congo Cratons during the Brasiliano/Pan-African orogeny that forged western Gondwana (de Brito Neves & Fuck, 2013).

Patagonia is a Neoproterozoic block that was added during the formation of the Pangea supercontinent (Pankhurst et al., 2006). Together with the South American Platform, Patagonia constitutes the stable part of the continent. Wide areas of the South American continent are covered by Phanerozoic sedimentary basins (Milani & Thomaz Filho, 2000). The Andean foreland basins cover the area eastwards adjacent to

the Andean chain. The Solimões and Amazon Basins cover wide areas of the Amazon Craton along the Amazon River in W-E direction, splitting the craton into the Guyana (north) and Guaporé Shields (south). Eastwards, the Parnaíba Basin covers the cratonic fragment of the same name (de Castro et al., 2014) between the Amazon (west), São Luis (north), and São Francisco (east) Cratons. Southwest of the São Francisco Craton and adjacent Tocantins tectonic province, the Paraná and Chaco-Paraná Basins spread toward the Andes and their foreland basins. The passive eastern margin of the continent exhibits a range of deep sedimentary basins, of which several are rich in carbon hydrogens and therefore well studied (Milani & Thomaz Filho, 2000).

1.2. Modeling Approach

An integrated, iterative approach based on topography, gravity, seismic, and mineral physics data is used to model composition, temperature, and density of the upper mantle in three dimensions (Kaban et al., 2014; Tesauro et al., 2014a). The method employs three principal steps. In the first step, seismic data on the crustal structure are used to calculate the residual mantle gravity field and residual topography, which mainly reflect the effect of density variations in the mantle. To achieve this, a crustal model that describes the thickness and density of the main layers (sediments and crystalline crust) is constructed, based on available seismic data, excluding previous crustal models based solely on gravity data (Section 2). Densities are obtained by conversion of seismic velocities, using non-linear equations (Christensen & Mooney, 1995) for the crystalline crust and the Gardner relation (Gardner et al., 1974) for sediments. The resulting crustal model is used to remove the crustal effect from the observed gravity field. In this way, it is also possible to calculate the residual topography that shows which parts of topography/bathymetry are over- or undercompensated by the crustal structure in an isostatic sense (Kaban & Mooney, 2001). To restrict the residual fields to those caused by changes in the upper mantle down to 325 km, the fields are also corrected for the anomalies originating from the deeper mantle based on global dynamic models.

In the second step, an initial thermal model of the upper mantle is constructed based on seismic tomography constrained by mineral physics, initially representing a juvenile, "fertile" mantle of uniform composition (Section 3). The model extends vertically from the Moho down to 325 km in slices of 50 km thickness at a lateral resolution of 1° × 1°, with the first slice extending from the Moho to 75 km depth. The chosen maximum depth should exceed the maximum lithospheric thickness of South America (e.g., Steinberger & Becker, 2018). The corresponding density variations are used to determine the temperature dependent gravity and dynamic effects of the mantle layers. After the residual mantle fields are corrected for these effects, it is assumed that the residuals primarily reflect variations of upper mantle composition and still unknown density variations within the crystalline crust. Finally, these residual fields are jointly inverted to assess necessary compositional density changes and the respective changes in composition are applied to the initial mantle model. A new thermal model is calculated and employed to improve the thermal corrections of the residual fields. Subsequently, this process is repeated iteratively until convergence is reached, yielding the final self-consistent variations of temperature, density, and composition (Section 4). As a result, a consistent 3D model of the uppermost mantle is obtained showing temperature and composition induced density anomalies as well as variations of these parameters. The method has been extensively tested (Kaban et al., 2015) and was applied for studies of North America, Eurasia and Antarctica (Haeger et al., 2019; Kaban, et al., 2016; Tesauro et al., 2014a).

2. New Model of the Crust and Residual Mantle Anomalies

A new model of the crust, including depth to the Moho, sediment thickness and density, was compiled based on available data in order to correct the observed gravity field for the crustal effect and to calculate residual topography.

2.1. Density Model of the Sedimentary Cover

In general, the structure of sedimentary basins is often complex and local features change over short distances. Yet, resolving such small features is not possible on the 1° × 1° scale of this study. However, since the aim of the density model is to provide a reasonable basis for estimation of large-scale gravity effects of
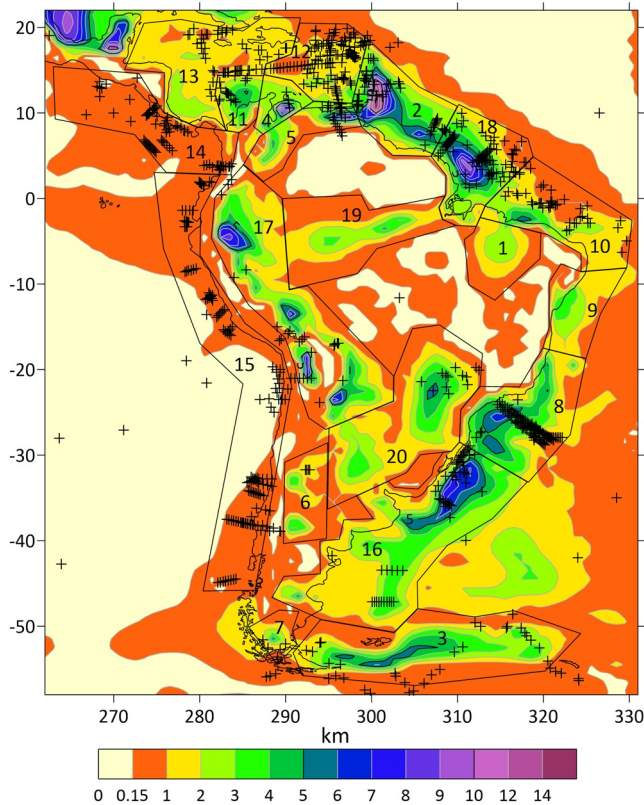
Figure 2. Thickness of sediments for South America and surroundings (Laske et al., 2013 after Exxon Production Research Company, 1985). Numbered polygons denote the different sediment basin areas. Crosses mark seismic data points from which P-wave velocities of sediments are available. Note the lack of data in the Parnaíba (polygon 1), Amazon and Solimões Basins (polygon 19) and offshore eastern Brazil (polygon 9).

the sedimentary cover, studying small-scale features is more suitable for local studies. Here, generalized density-depth relations were constructed which characterize each specific basin, following Stolk et al. (2013). Locations of seismic measurements, thickness of sediment layers and P-wave velocities in each of them were extracted from the GSC (Global Seismic Catalog, Mooney, 2015 with updates up to 2019). Total sediment thickness (Figure 2) was taken from the CRUST1.0 model (Laske et al., 2013), which was digitized from the Exxon tectonic map of the world (Exxon Production Research Company, 1985). In a first step, sedimentary basins were defined based on total thickness of sediments. Borders were placed in areas of thin sediment coverage and in accordance with Milani and Thomaz Filho (2000). Since the seismic data are distributed irregularly across South America and its surroundings, data coverage varies strongly across distinct basins. Therefore, smaller basins and those comparable in structure and genesis were combined to increase the amount of available seismic data for each basin. This approach led to a total number of 20 different sedimentary basin areas of which only three do not contain seismic data (Figure 2; polygons 1, 9 and 19).

In a sedimentary basin, density and P-wave velocity increase with depth due to lithostatic compaction, while the rate of compaction decreases with depth. Therefore, the increase of P-wave velocities can be described by a capped exponential equation:

$$V_p(z) = V_{max} - (V_{max} - V_{surf}) \cdot e^{B(-z)}$$

In the above equation, V_{surf} is the surface P-wave velocity (km/s). V_{max} was set to 6 km/s which is assumed to represent maximum compaction of sediments. The parameter B describes the compaction (1/km) of sediments with depth z in kilometers.

Before calculating the velocity-depth relation in each basin, layer thicknesses given in the database were converted to middle-of-layer depths. In the next step, data were sorted to the respective basin polygons and binned to 100 m depth intervals to reduce the effects of outliers. The average velocity of each bin was placed at its center. Parameters V_{surf} and B from the above equation were determined for each polygon using least-squares regression (Figure 3).

Assuming that the velocity-depth structure of any basin is known, P-wave velocities can be converted to densities by means of the relations proposed by Gardner et al. (1974) or Nafe and Drake (Ludwig et al., 1970):

$$\rho_{Gardner} = 1.74 \cdot V_p^{0.25}$$

$$\rho_{ND} = 1.6612 \cdot V_p - 0.4721 \cdot V_p^2 + 0.0671 \cdot V_p^3 - 0.0043 \cdot V_p^4 + 0.000106 \cdot V_p^5$$

In this work, Gardner's rule was used to transform the resulting velocity-depth relations into density-depth relations (Figure 3).

Different solutions were found for the three polygons missing data and the onshore and offshore regions outside the polygons, respectively. The data gap in the Parnaíba Basin (Figure 2; polygon 1) was filled using data from borehole measurements (de Castro et al., 2016). Two logging profiles enabled using the approach described for the other basins. The density depth relation from Silva et al. (2006) was used for the uncovered area offshore eastern Brazil (Figure 2; polygon 9). A density depth relation based on S-wave velocities converted to P-wave velocities (Brocher, 2005) was used for the Amazon Basin (Figure 2; polygon 19). Since most of the onshore areas outside the basin polygons are of cratonic origin, they were assigned the densi-
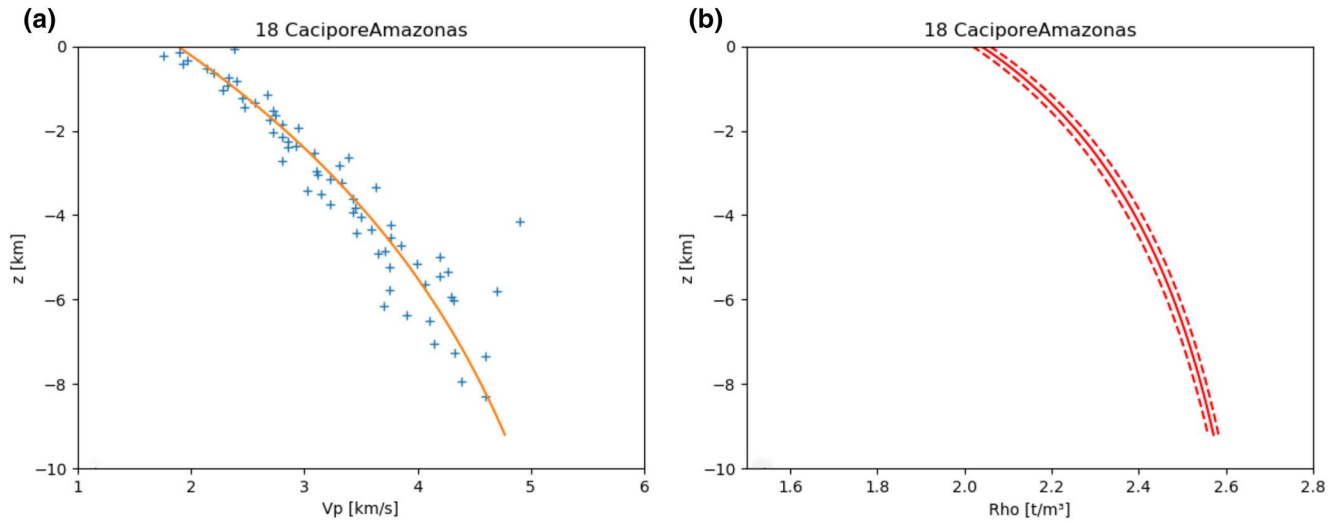
Figure 3. Results for basin no. 18, which is well covered by seismic data. Left: Velocity-depth relation curve. Blue crosses are binned data. Right: Density-depth relation for the basin. Dashed lines represent the 1σ uncertainty interval.

ty-depth relation calculated for the cratonic Paraná and Chaco-Paraná Basins (Figure 2; polygon 20). The following density depth relation from Kaban and Mooney (2001) was used for the offshore areas outside the polygons:

$$\rho(z) = \begin{cases} 2.00837 + 0.3734z - 0.8414z^2 + 0.00794z^3 - 0.0002602z^4, & z \leq 4.2\,\text{km} \\ \rho(4.2) + \left(2.67 - \rho(4.2)\right)\dfrac{z - 4.2}{18 - 4.2}, & z > 4.2\,\text{km} \end{cases}$$

2.2. Initial Model of the Crystalline Crust

The existing seismic determinations (Mooney, 2015 with updates up to 2019) are very heterogeneous for South America with respect to thickness of the crystalline crust layers and their seismic velocities. Therefore, it was not possible to construct a consistent model of the crystalline crust as it was done for North America and Eurasia (Stolk et al., 2013; Tesauro et al., 2014b). Moreover, even the vertically averaged P-wave velocities within the crystalline crust, which are usually more stable, are sparse and show regular patterns only for some tectonic provinces (Figure 4a). The central Andes are characterized by significantly reduced average Vp (about 6.14 km/s) with a gradual increase to the north and south. In contrast, relatively high velocities (up to 6.6 km/s) were reported earlier by Mooney et al. (1979) for the Northern Andes (Western Cordillera). A part of the Paraná Basin is also characterized by increased velocities (6.56 km/s).

Therefore, it was decided to not create a detailed model of the crystalline crust, but to initially construct a generalized model that only keeps well-defined features. In addition, relatively high velocity values for the Chaco-Paraná Basin are kept on account of its structural similarity to the Paraná Basin. For the rest of the continent, we assign a standard value of 6.45 km/s, which is typical for continents (e.g., Christensen & Mooney, 1995; Tesauro et al., 2014b). For the oceanic area (outside shelf), the value 6.54 km/s is taken (Figure 4b). Later, this model is improved by the inversion of the residual gravity and topography together with the adjustment of the initial upper mantle model. The average velocity variations within the crystalline crust, which are adopted for the initial model, are shown in Figure 4b. The velocities have been converted to densities by applying non-linear relationships from Christensen and Mooney (1995). For calculations, which require global distribution of all parameters, the crystalline crustal model of South America has been embedded into the global one.
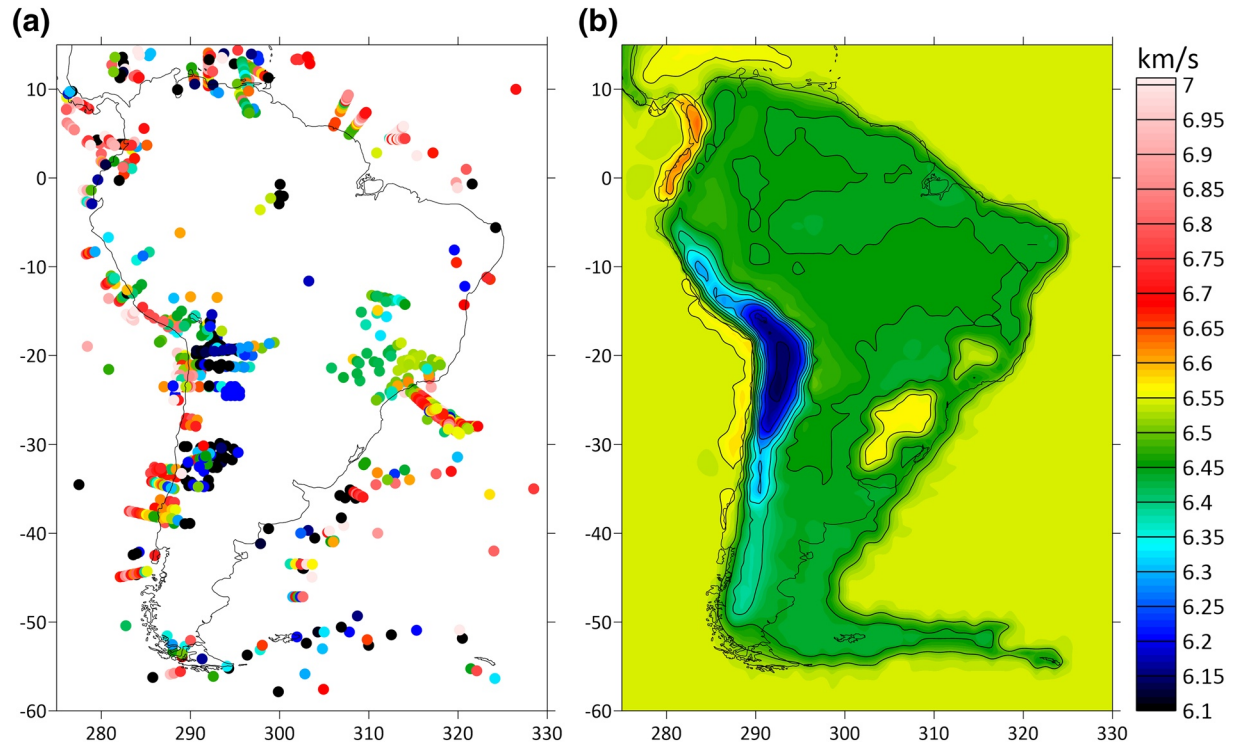
Figure 4. Vertically averaged P-wave velocities within the crystalline crust. (a) Colored dots show seismic determinations from the GSC (Mooney, 2015 with updates up to 2019). (b) Generalized initial model of the crystalline crust.

2.3. Depth to the Moho

Several models of crustal thickness (including topography/bathymetry) and depth to the Moho (relative to sea level) of South America have been published over the past years. The most recent one was published by Rivadeneyra-Vera et al. (2019), who added several hundred new seismic measurements to the data set of Assumpção et al. (2013) based on new seismic stations and previous studies. Unfortunately, both models also contain gravity-derived crustal thicknesses in areas like the sub-Andean range (Tassara & Echaurren, 2012) and Ecuador (Araujo, 2013; Font et al., 2013). Several gravity-derived models were published as well (Haas et al., 2020; Uieda & Barbosa, 2017; van der Meijde et al., 2013), but solely seismic determinations of depth to the Moho are desired in the employed approach. This way, an unintentional removal of parts of the mantle gravity signal is avoided as it would occur if the initial gravity field was inverted for depth to the Moho. Seismic data from the recent publication of Rivadeneyra-Vera et al. (2019) were augmented with those from the GSC database (Mooney, 2015 with updates up to 2019). Determinations were binned to $1° \times 1°$ cells corresponding to the final resolution of the model. Interpolation of depth to the Moho was done following the remove-interpolate-restore method introduced by Stolk et al. (2013). In this method, the measurements of depth to the Moho are corrected for the effect of adjusted topography (h_{adj}), which would be the height of topography if water and sediments were condensed to the density of topography (Amante & Eakins, 2009), which was chosen as $\rho_{topo} = 2.67$ g/cm^3. This allows to remove the first-order effect of surface loading by topography, water and sediments from the depth to Moho measurements assuming local Airy Isostasy:

$$M_{res} = M_{obs} - \frac{\rho_{uc}}{\Delta\rho_{Moho}} \cdot h_{adj}$$

Here, $\rho_{uc} = 2.67$ g/cm^3 is the density of the upper crust and $\Delta\rho_{Moho} = 0.47$ g/cm^3 is the assumed density contrast across the Moho. It has been shown that the residual depths to Moho are much less variable, which simplifies their interpolation (Stolk et al., 2013).
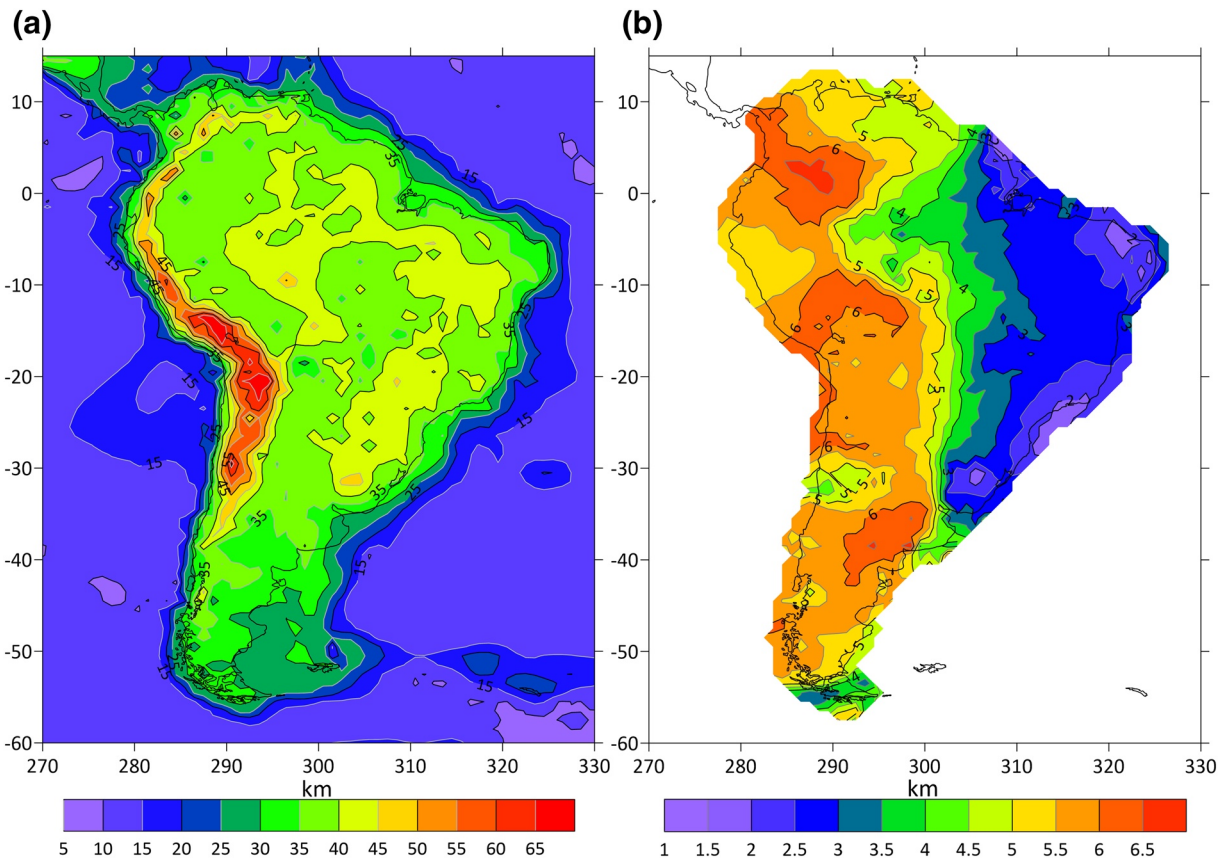
Figure 5. a) Final map of depth to Moho. Observations at stations were treated as exact and restored after interpolation. (b) Uncertainty of depth to Moho interpolation. Note the trend of uncertainties increasing from east to west, due to differences in data density and heterogeneity of tectonic structures.

Depths to the residual Moho were interpolated using Ordinary Kriging by means of the Python module PyKrige (Murphy et al., 2020), which also provides statistical interpolation uncertainties. Data given to the estimator were restricted to a 10° radius around each interpolation point. Points with less than 11 surrounding data points in the given range were omitted in the interpolation, which is the minimum number of points necessary to achieve stable results (Stolk et al., 2013). Interpolation was also carried out for each data point without using the point itself for cross validation. Afterwards, two subsets of the point data were created: The first contained the data points where the difference between observed and interpolated values was smaller than, or equal to, two times the standard deviation σ ("inliers"), while the second subset contained the remaining points ("outliers"). Interpolation was repeated for the outlier points using inlier data only. Points fulfilling the 2σ criterion after recalculation were added to the inlier subset which was used for the final interpolation of depth to the Moho, while the remaining outliers were discarded. This way, the cross validation does not only allow to remove outliers but also to rehabilitate points that were falsely flagged as outliers after the first interpolation due to the distorting effects of surrounding outliers. Since the measured data points are overall more credible than interpolation results, they were treated as "exact" in the final interpolation. Afterwards, the isostatic correction was restored by adding the correction term $\frac{\rho_{uc}}{\Delta\rho_{Moho}} \cdot h_{adj}$ back to the resulting field. Thus, the original values are completely restored in the final map, while the depth to the Moho follows main features of the adjusted topography (e.g., mountain ranges) in the interpolated regions. Finally, the results were merged into the global depth to Moho grid.

Figure 5 shows the final map of the interpolated depth to the Moho (a) and its uncertainties σ (b). The latter is based on the interpolation uncertainties, since the database of crustal structure does not provide them for

most of the measurements. In addition, the interpolation uncertainty is usually larger than the measurement accuracy for the same point and can thus be considered as an absolute upper error boundary.

In general, the cratonic regions are characterized by depths to the Moho of more than 40 km. Thick crust extends south of the São Francisco Craton under the Paraná Basin and is also found under the Parnaíba Basin in northeastern Brazil. A corridor of slightly shallower depths to the Moho is found roughly along the TBL between the Amazon and São Francisco Cratons. Depth to the Moho is up to 70 km in the central Andes and between 40 and 60 km further north. South of 30°S, the root of the Andes is not visible in the Patagonian Domain. Overall, depths to the Moho of less than 35 km dominate in the Patagonian Domain. The few data points in the Andean forelands indicate extended crust east of the Andes with depths to the Moho less than 35 km due to backarc extension. However, the surrounding interpolated values indicate depths to the Moho around 37 km. This is probably a slight overestimate arising from the heterogeneous data distribution and the sharp transition from the thinned foreland crust to the thick crust characterizing the adjacent Andes and Amazon Craton.

Interpolation uncertainties show an increasing trend from low values in the eastern coastal areas (<2.5 km) to high uncertainties along the Andes and their forelands in the west (up to 6.6 km), probably due to several reasons. First, differences in depth to the Moho between the foreland areas and mountain ranges are high (up to 30 km) and occur over short distances introducing strong gradients. Second, the crust thickens again towards the cratonic areas further east, spatially limiting the minimum in depth to the Moho. At the same time, data coverage is high in the Andes and low in the forelands. Therefore, the maxima in the Andes strongly influence interpolation of foreland minima, leading to higher uncertainties. Moreover, measured depths to the Moho vary strongly in the Andes, further enhancing interpolation uncertainty.

2.4. Residual Mantle Gravity Anomalies and Residual Topography

In the next step, residual gravity anomalies and residual topography have been determined by removing the crustal components from the observed fields. The initial gravity field is based on the Eigen-6C4 model (Förste et al., 2014), which was downscaled to the resolution of the present study (1° × 1°). It represents a combination of satellite data (chiefly GRACE and GOCE satellites) and existing ground/airborne measurements. However, the long-wavelength part used here (up to ~180 spherical harmonic degree/order) is fully based on the satellite data. Therefore, the initial gravity field is homogeneous and equally presented in the whole area independent from the ground observations.

The gravity effect of the crustal layers including topography/bathymetry has been estimated relative to a 1D reference model following the approach employed previously in global (Kaban et al., 2003) and regional studies (Kaban et al., 2010, 2014, 2016; Mooney & Kaban, 2010). The reference model consists of an upper (0–15 km, 2.7 g/cm³) and lower (15–40 km, 2.94 g/cm³) crustal layer overlying an upper mantle layer (40–75 km, 3.35 g/cm³). This enables the direct comparison of the residual anomalies obtained for different regions. It has been shown that possible changes of the reference model mainly lead to a constant shift of the estimated residual anomalies and, therefore, are of little importance for the purposes of this study (e.g., Mooney & Kaban, 2010). Initially, the density of topography was set to 2.67 g/cm³. Later, when computing the relative effect of sediments, it was corrected accordingly. The effect of bathymetry was calculated for a water density of 1.03 g/cm³. The gravity anomalies of each layer have been computed with a 3D method on a spherical Earth; for details see Kaban et al. (2016). As was mentioned above, the gravity effect at each point was calculated taking into account the global distribution of all parameters. Total effect of the crust (including topography/bathymetry) is shown in Figure 6b together with the initial free air anomalies (Figure 6a). The crustal field is centered by removing the average of the area in Figure 6. It is obvious that these fields are very different. Intracontinental areas are mostly characterized by significant negative anomalies due to the thick crust, low density sediments, and reduced density of the crystalline crust in the Central Andes. Therefore, large density anomalies still exist in the crystalline crust and upper mantle.

Residual gravity anomalies were obtained after removing the gravity effect of the initial crustal model from the observed field. Additionally, the effect of deep density variations below 325 km (the bottom of the model) has also been removed from the observed field following the approach of Kaban et al. (2015) using a global seismic tomography (S40RTS, Ritsema et al., 2011). Therefore, the calculated residual gravity field
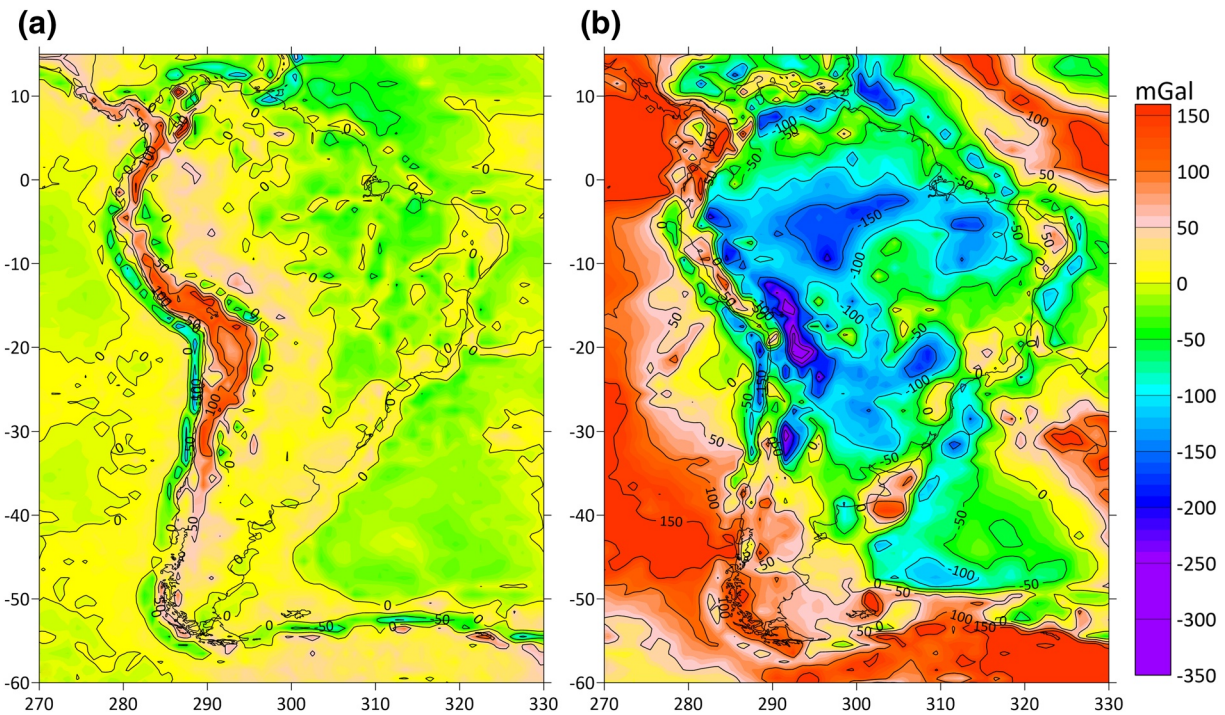
Figure 6. (a) Free air gravity anomalies (disturbances) according to the model Eigen-6C4 downscaled to 1° × 1° (Förste et al., 2014). (b) Gravity effect of the crust including topography/bathymetry relative to a 1D reference model (see text for details).

(Figure 7a) should mainly reflect the effect of density variations within the uppermost mantle and crystalline crust. Possible uncertainties of the residual gravity were extensively discussed in previous works (Kaban et al., 2016; Mooney & Kaban, 2010). Yet, these estimations would be inadequate in the case of South America, since potentially large gravity effects might be related to non-constrained density anomalies within the crystalline crust, which significantly exceed the uncertainties related to the sedimentary cover and Moho. However, the subsequent inversion allows to correct the initial crustal model.

The initial crustal model has been further employed for calculation of the residual topography, representing the part of the surface topography/bathymetry, which is not isostatically balanced by the crustal density heterogeneity. As for the residual gravity field, the dynamic effect of deep density variations below 325 km has been removed. The obtained field is shown in Figure 7b. As mentioned above, inversion of both parameters provides a possibility to resolve the vertical distribution of density variation much more reliably than by using only one field.

Gravity residuals are in the range of ±100 mGal for most of the South American Platform and the Andes. Positive residuals above 100 mGal occur under the Parnaíba Basin in northeast Brazil and along the Amazonas. Highest positive residuals are found in the central Andes, reaching up to ∼250 mGal. Negative residuals span along the eastern coast of the continent, including wide parts of the São Francisco and Paranapanema Cratons as well as the whole Rio de la Plata Craton. In contrast, negative residuals at the Amazon Craton are limited to smalls parts of the central Guaporé Shield and northern rim of the Guyana Shield. Residuals in the Patagonian domain are strongly negative, partially <−150 mGal.

Residual topography is anticorrelated to gravity residuals. The stable cratonic platform shows values mostly below 2 km. The regions of strong positive gravity residuals under the Parnaíba and Amazon Basins are marked by residual topography below 1 km. Values above 2 km are found in the areas of negative gravity residuals, but are mostly limited to parts of the Paraná Basin as well as southern São Francisco and Rio de la Plata Cratons. The northwestern coastal area and Patagonia exhibit values >2.5 km. Almost no negative anomalies are present, except for the central Andes, which are characterized by values down to some −3 km, and very small parts of the Parnaíba and Paranapanema Basins.
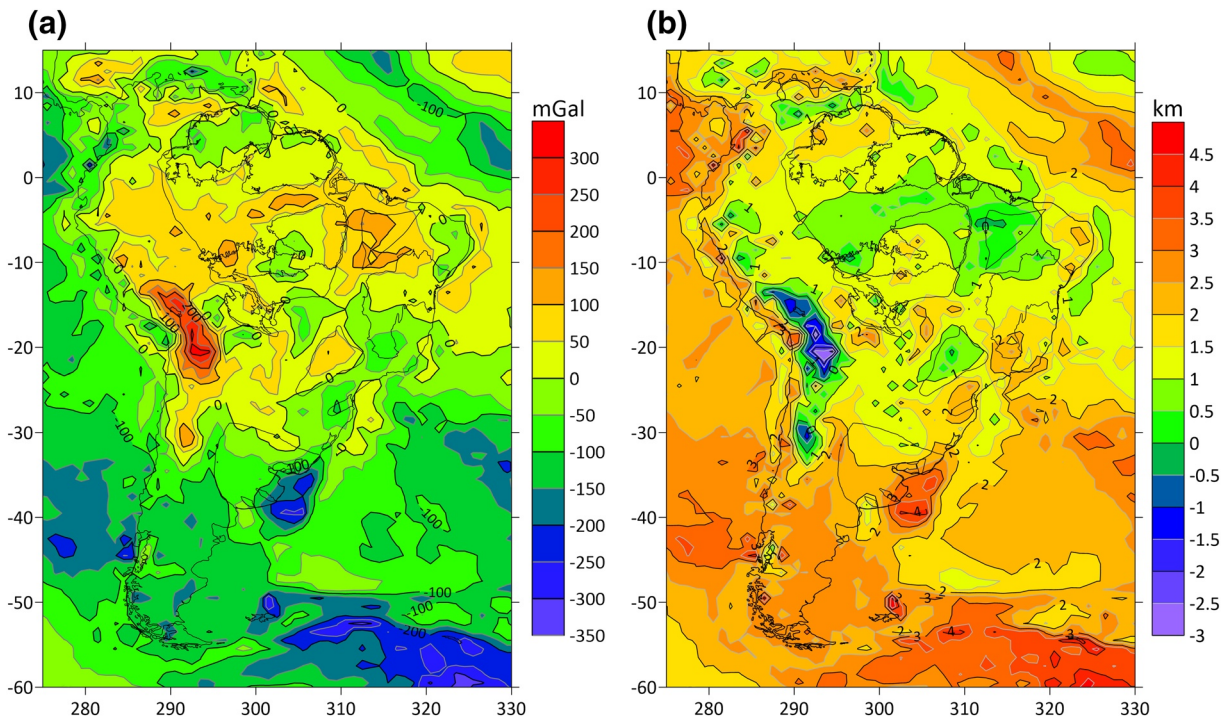
Figure 7. Residual mantle gravity (a) and residual topography (b) after correction for respective effects of the crust and deep mantle. Residual topography is shown for the common reference density of 2.67 g/cm³. Note the apparent anticorrelation of the two fields.

3. Initial Thermal Model of the Upper Mantle

Density anomalies in the upper mantle are assumed to be mainly caused by thermal and compositional effects. While lower temperatures in old rock assemblies cause positive gravity anomalies in the upper mantle, compositional variations due to reduced iron content have the opposite effect. Calculating the thermal effects of the assumed mineral assembly on density allows to refine compositional anomalies in the residual fields.

3.1. Method

Employing the method of Tesauro et al. (2014a), a juvenile, "fertile" mantle composition is assumed for the initial thermal model, consisting of Olivine (58.5%), Clinopyroxene (11.5%), Orthopyroxene (15%), and Garnet (15%), where Garnet is always assumed to contain 20% of its Ca-endmember Grossular. This composition was chosen according to that of xenoliths (Griffin et al., 2003; McDonough & Sun, 1995). Besides temperature and pressure, density and other physical properties, for example, elastic parameters, depend on the mineral composition and the amount of Mg content with respect to that of Fe, which is expressed by the Mg number (Mg# = 100 × Mg/(Mg + Fe)). The Mg# of the initially assumed juvenile mantle composition mentioned above is 89. Using mineral physics equations (Stixrude & Lithgow-Bertelloni, 2005) as described in detail in Tesauro et al. (2014a), density ρ and shear modulus μ of the minerals are estimated for temperatures up to 1800°C and respective lithostatic pressure (Dziewonski & Anderson, 1981) in each depth interval. The volumetrically weighted mineral densities are summed up to retrieve bulk rock density. Shear modulus of the bulk rock is calculated by Voigt-Reuss-Hill averaging of the minerals' respective moduli. Then, anharmonic synthetic S-wave velocities are determined for all temperatures and each depth interval using the relation $V_s = \sqrt{\mu / \rho}$. Model Q3 from Cammarano et al. (2003), which is assumed to best represent the "dry" conditions of old cratonic lithosphere (e.g., Hirth et al., 2000; Novella et al., 2015), is used to calculate the dampening effect of anelasticity in the platform area (Figure 1, white outline). The model Q4, assuming "wet" mantle conditions, is used for the other areas. Finally, temperatures and densities are de-

termined by finding the synthetic S-wave velocities that best fit the absolute values from the recent regional seismic tomography model SA2019 (Celli et al., 2020) in each grid cell. The densities are normalized to show variations around the global mean and enable correction of the residual gravity field and residual topography for thermal effects. Thus, it can be assumed that remaining anomalies are to the first order induced by compositional variations.

3.2. Results

Although calculated fields exist up to a depth of 325 km, estimated temperatures and their effects on density are only shown for the depths up to 200 km (Figure 8), since this is the part of the mantle, where significant heterogeneities occur (e.g., Schaeffer & Lebedev, 2013). At 50 km depth, seismic velocities and resulting temperatures might be biased by incorrect Moho positioning in the tomography model or the deep crustal roots present in some parts of the area (e.g., the Andes). Thus, they could mislead interpretations and are not shown either.

As expected, temperatures (Figure 8, left column) and temperature-induced density variations (Figure 8, right column) are strongly anticorrelated. In general, old cratonic regions show lower temperatures than their surroundings. Temperatures are <1000°C at a depth of 100 km in the Amazon, Parnaíba, São Francisco and Paranapanema Cratons, with minima <700°C. They remain below 1100°C down to a depth of 200 km at the central Guaporé and eastern Guyana Shields, and at the São Francisco and eastern Paranapanema Cratons as well. In these regions, thermal density variations range from up to 0.05 g/cm³ at shallower depths to 0.01 g/cm³ at 200 km, indicating the proximity of the bottom limit of the deep lithospheric roots. Although temperatures in the Parnaíba and São Luis Cratons exceed 1200°C at 200 km depth, the temperature induced density variations are still above zero. At the RoSS, the western Guyana Shield and northern Solimões Basin, temperatures are >1100°C at 150 km and well above 1300°C at 200 km with thermal density variations between 0.01 and −0.02 g/cm³, respectively. The thermal density variations are negative through all depths at the Luiz Alves and Rio de la Plata Cratons, which already show temperatures >1200°C at a depth of 100 km. The lithosphere is probably thin in these areas with temperatures >1300°C at 200 km, including the Andean Forelands and most areas along the TBL, where thermal densities are negative at all depths as well. However, since this is only the initial model, the results are not further discussed here.
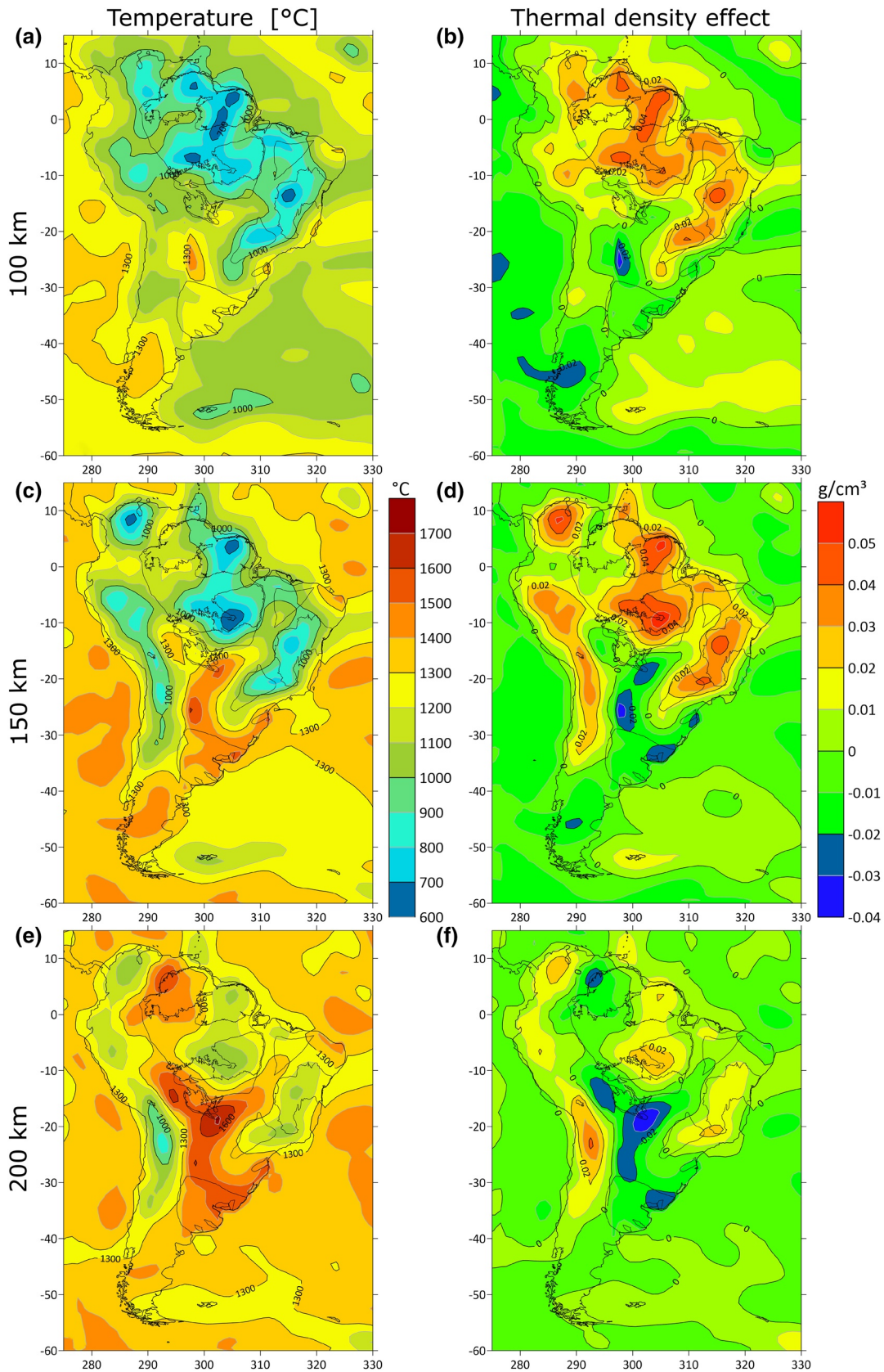
4. Inversion and Iterations

4.1. Method

Gravity and dynamic effects of the depth slices are calculated based on the temperature-induced density variations (Chapter 3) and enable correction of the residual mantle gravity and residual topography for respective effects. The thermally corrected fields are then jointly inverted to obtain density variations in the uppermost mantle and crystalline crust. The great advantage of using both the gravity field and residual topography lies in their different dependence on the distribution of density heterogeneities (Kaban et al., 2015). This allows to reduce the principal ambiguity compared to interpretation of only one parameter, where the outcome would heavily depend on the starting parameters of the inversion. Thus, a more realistic 3D density distribution can be modeled by minimizing

$$\left\| A\rho - g_{res} \right\|_2 + k^2 \left\| B\rho - t_{res} \right\|_2 + \alpha \left\| \rho - \rho_{ini} \right\|_2$$

Here, A and B are the operators that transform density to gravity and dynamic topography, respectively. To normalize topography with respect to gravity, the second term is multiplied by the factor $k = 2\pi G\rho_{topo}$. Based on viscosity, the inversion code calculates full dynamic effects of the mantle density variations as a part of the residual topography signal (t_{res}, Kaban et al., 2015). The third expression is a regularization term requiring that the resulting density model does not differ too strong from the initial model ρ_{ini}. In the present study, it is set to zero to keep density variations minimal. Damping is controlled by $\alpha = 2\pi GD_n$ with the damping parameter D_n set to 0.83, based on previous studies (e.g., Haeger et al., 2019). Tests with synthetic models showed that the exact choice of D_n has an insignificant effect on the inversion results while in the range of 0.5–1.2 (Kaban et al., 2015). For further tests of the method's reliability, the interested reader is

referred to Kaban et al. (2015). The inversion is done in spherical harmonics which requires global grids of the respective fields.

The output of these calculations consists of slices of density perturbations at the same depths, for which temperature and thermal effects were calculated. An additional slice centered at a depth of 15 km is added on top to account for additional density variations in the crystalline crust not present in the initial model. Since the mantle perturbations are to the first order thought to represent compositional density variations (Chapter 3.1), they can be converted to changes in Mg#. With the initial model representing a juvenile, undepleted mantle, it is not admissible to further lower the Mg#, i. e., increase the iron content and thus the density of the mineral assembly. Therefore, only negative values of the output are considered as implying a positive change of the Mg# with respect to the initial value of 89. On average, a density change of $\Delta\rho = -0.01625\,\text{g/cm}^3$ equals an increase of Mg# by 1. The compositional changes discussed here are limited to the area of interest, which corresponds to the South American Platform (Figure 7, white outline). The Mg# is changed towards a depleted mantle with Mg# 94 and respective composition (69.5% Olivine, 4% Clinopyroxene, 21% Orthopyroxene, and 5.5% Garnet) to comply with the inversion output. Compositions between the endmembers, represented by Mg# 89 and Mg# 94, are interpolated linearly due to lack of further constraints. Using the new compositional model, the temperature model is updated. The whole procedure of temperature calculation, correction for its effects, and inversion for compositional changes is repeated until convergence is achieved. This is the case when the resulting fields of Mg# of two consecutive iterations do not show any difference greater than 0.1. In the present study, the scheme converged after at most four iterations.
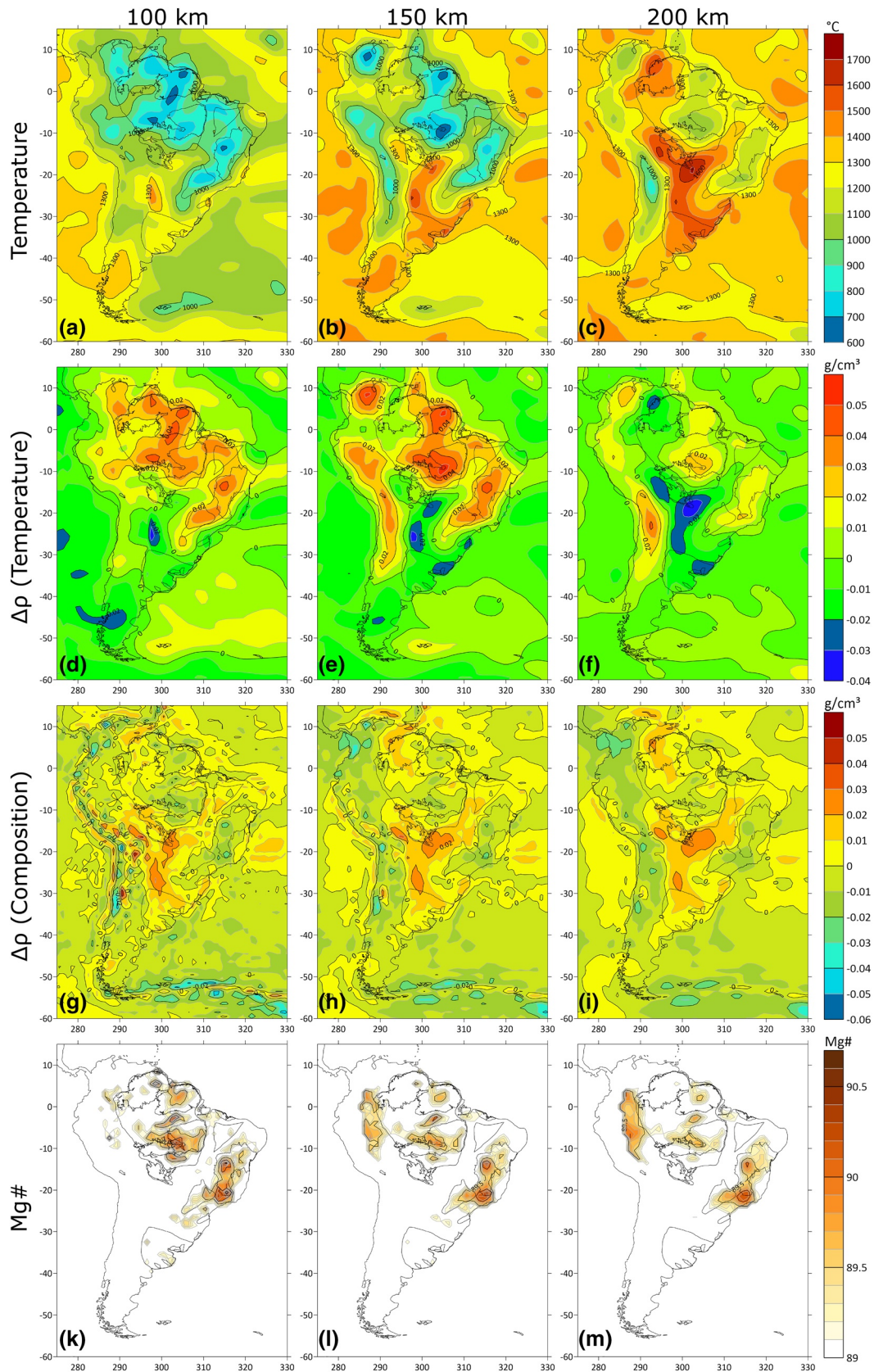
4.2. Final Results of Temperature, Density, and Composition

As for the initial temperature model, the results of the final iteration are presented for the depths of 100, 150, and 200 km (Figure 9, columns). They show temperature, temperature- and composition-related density variations and Mg# (Figure 9, rows). Differences between the initial temperature model and final iteration are rather small. Furthermore, they are limited to the areas of iron depletion, since a change in composition is necessary to induce changes to the initial model. The final iteration shows less than 60 K higher temperatures in those areas, altering temperature dependent density variations by less than 0.005 g/cm^3. Thus, general patterns and structures described in Chapter 3.2 are not changed significantly through the iterative process. The results for the compositional density variations are generally anticorrelated with those induced by temperatures. As expected, negative anomalies are mostly present in the areas of low temperatures and respective positive thermal density variations.

In the Amazon and São Francisco Cratons, the low temperatures and positive thermal density variations are accompanied by negative compositional anomalies through all depths, which are interpreted as due to iron depletion. In wide regions of both cratons, temperatures remain low through iterations and cause positive thermal density variations (Figures 9a–9f). In depths >= 150 km at the Amazon Craton, they are limited to the central Guaporé to eastern Guyana Shield (Figures 9b, 9c, 9e, and 9f). Compositional density variations are mostly negative in these areas, ranging from some −0.02 g/cm^3 at 100 km up to almost zero at 200 km (Figures 9g–9i). Values of Mg# of up to 90.4 are found at 100 km depth, decreasing to less than 90.1 at 150 km and 89.8 at 200 km depth (Figures 9k–9m). The negative compositional anomalies in the Guyana Shield are mostly restricted to its eastern and northern parts northwest of the Amazonas Delta with slightly lower Mg#. The western Guyana Shield and northern Solimões Basin show significantly higher temperatures at depths of 150 (>1100°C) and 200 km (>1300°C). Correspondingly, thermal density variations are negative and compositional ones are positive. The southwestern part (RoSS) of the craton exhibits high temperatures (>1000°C at 100 to >1400°C at 200 km depths) through all depths and no depletion.

The São Francisco Craton shows minimal temperatures (<700°C) at the center of its southward bend at 100 km depth. In general, they remain below 1200°C down to the depth of 200 km, with corresponding

Figure 8. Temperatures (left column) and thermal density variations (right column) from the initial model at depths of 100 (a and b), 150 (c and d), and 200 km (e and f). Temperatures are low at most of the AMZ, Pp and SF through depths with concurrent positive thermal density variations. Higher temperatures and respective negative density variations dominate the RdP, LA, TBL, and Andean Forelands.

positive thermal density variations. These are accompanied by compositional anomalies partially below −0.02 g/cm³ through all depths, inducing Mg# values of up to 90.7 at 100 km depth to 90.2 at 200 km depth. From the southern tip of the craton, low temperatures and negative compositional anomalies stretch further southwest under the Paraná Basin, where the Paranapanema Craton is located. Here, temperatures remain as well mostly below 1300°C up to 200 km depth. With increasing depth, the low temperature zone and its minimum are shifted towards the São Francisco Craton, leaving only the eastern part of the Paranapanema Craton with temperatures less than 1200°C at 200 km. Here, negative compositional anomalies imply values of Mg# up to 89.8 through all depths, which increase toward the São Francisco Craton. The respective compositional density minimum and maximum Mg# are located at the southern end of the São Francisco Craton. Depletion is also indicated at the center, southern end and south of the Paranapanema Craton, where the Paraná Flood Basalts are emplaced. Compositional densities do not exceed −0.01 g/cm³ through depths with Mg# up to 89.5. Anomalies south of the craton shrink with increasing depth while the others indicate that the areas of depletion are concatenated with those at the southern end of the São Francisco Craton.

At the southern end of the region of interest lies the Rio de la Plata Craton with its large hypothesized subsurface extent. In this area, temperatures are very high (close to 1400°C at 150 km depth), inducing negative temperature dependent density variations. Some small negative compositional variations (>−0.01 g/cm³) are suggested close to the coast at a depth of 100 km, implying values of Mg# <89.2. At the Luiz Alves cratonic fragment northeast of it, estimated temperatures are also high (>1400°C at 200 km), without indications for negative compositional anomalies. Low temperatures at the São Luis cratonic fragment in northeastern Brazil (<1200°C at 200 km) are part of the low temperature zone of the Amazon Craton. No distinct compositional anomalies related to its shape are present, indicating absence of depletion. From the southern TBL, temperatures above 1300°C at 100 km extend towards the Parnaíba Basin with increasing depth, where another cratonic fragment is proposed to be covered by sediments. Here, temperatures are below 1300°C down to 200 km with respective positive thermal density variations. Yet, compositional density variations are positive, as they are along most of the TBL through all depths indicating absence of depletion. West of the Amazon Craton at depths >= 150 km, negative compositional anomalies indicate depletion (Mg# up to 90), despite high temperatures.

4.3. Improvement of Crystalline Crust Density Model

As mentioned in chapter 4.1, the model comprises an additional layer centered at 15 km depth to account for crustal density variations. Therefore, density variations not included in the initial model of the crystalline crust can be assessed, which allows to update the crustal density model as a useful byproduct of the iterative process (Figure 10). Negative density variations down to some −0.05 g/cm³ are indicated for most of the eastern part of the continent, including the Amazon and São Francisco Cratons. An increase of densities up to 0.026 g/cm³ is found at the Amazon Basin and along the southwestern border of the Amazon Craton down to the RoSS, as well as parts of the Parnaíba Basin and the northern São Francisco Craton (Figure 10b). Increased density and positive gravity residuals (Figure 6) at the Amazon Basin are consistent with magmatic intrusions in the lower crust proposed by Nunn & Aires (1988). The Andes and their Forelands exhibit even higher density variations, partially exceeding 0.05 g/cm³. The initial model (Figure 10a) included densities >2.875 g/cm³ for the southern São Francisco Craton and >2.9 g/cm³ for most of the Paraná Basin. A slight density decrease (up to −0.025 g/cm³) is indicated in the inversion results for these areas, except for the southernmost Paraná Basin, where an increase of up to 0.025 g/cm³ is found. A density increase is also suggested for the Paranapanema Craton and northern part of the proposed Rio de la Plata Craton (Figure 10b). In the resulting, adjusted crustal density model (Figure 10c), most of the stable South American Platform is characterized by densities between 2.85 and 2.9 g/cm³. Lower densities are found at the Guyana and Guaporé Shields, along the TBL and at the Andes (minimum of 2.77 g/cm³). Meanwhile, the Andean Forelands and the Paraná Basin exhibit higher densities with local maxima up to 2.93 g/cm³.

Figure 9. Results after the final iteration. Rows show the different fields of temperature (a–c), thermal density variations (d–f), compositional density variations (g–i) and composition in terms of Mg# (k–m) at depths of 100, 150, and 200 km, respectively. Color ranges match those of other figures to ease comparisons. Most cratonic areas are marked by low temperatures and positive thermal density variations, which are counteracted by negative compositional anomalies implying increased Mg#.
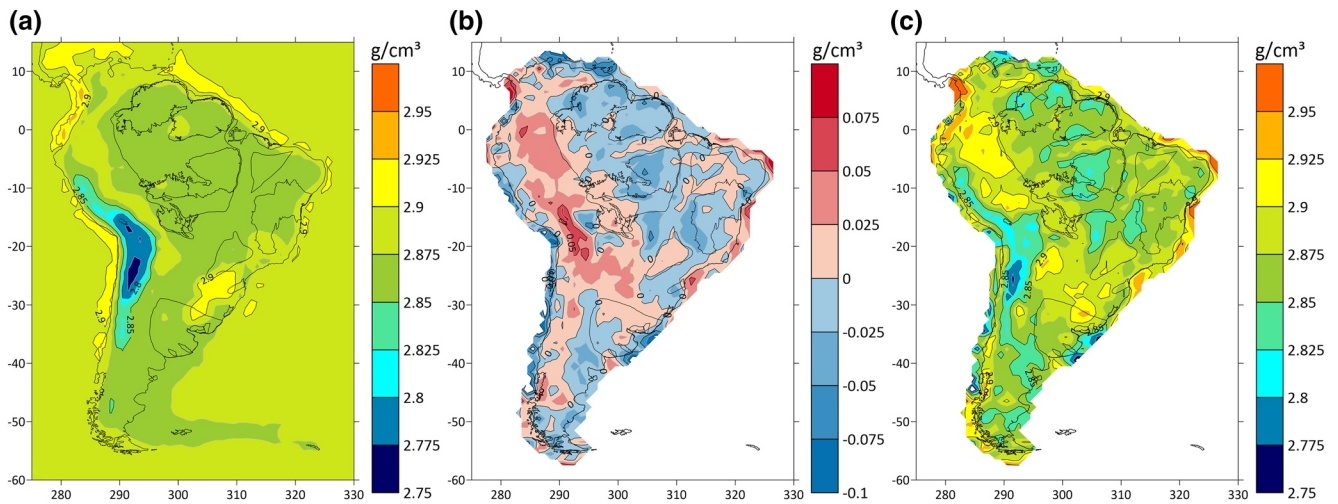
Figure 10. (a) Initial crustal density from conversion of seismic velocities in Figure 3. (b) Proposed change to average density of the crystalline crust resulting from the inversion. (c) Adjusted average density of the crystalline crust, colors as in (a).

5. Main Sources of Uncertainties

5.1. Seismic Tomography

The temperature model created in the iterative approach is based on S-wave tomography data and mineral physics and is affected by several uncertainties. These have been discussed in previous studies employing the method (e.g., Haeger et al., 2019; Tesauro et al., 2014a):

1. According to Lee (2003), an incorrect compositional model could cause a temperature error of up to 200°C in areas of high depletion, i. e., the cratons. In the given case, this value is significantly reduced since the compositional model is adjusted through iterations.
2. At temperatures above 900°C, attenuation becomes more effective. An incorrect model choice would result in an error of ~100°C (Jackson et al., 2002). As mentioned before, we use the attenuation models Q3, representative of "dry" lithospheric conditions, for the stable, mostly cratonic South American Platform and Q4, assuming "wet" conditions for the adjacent Andean Range and Patagonia, respectively (Cammarano et al., 2003). Therefore, respective uncertainties should be smaller in this study.
3. Uncertainties caused by the temperature derivatives of elastic parameters are estimated to be roughly 70°C (Tesauro et al., 2014a).
4. In addition, the chosen tomography model has a large impact. A change of temperature results by 100°C corresponds to a velocity change of about 40–60 m/s in the temperature range of 600–1000°C for the model Q3. This increases up to ~80 m/s at >1300°C, i. e., the impact of velocity uncertainties is a bit smaller at higher temperatures. Thus, the effects of uncertainties in the tomography model or corresponding differences between various models could amount to more than 200°C in the cool cratonic areas. The above estimated velocity variations that are necessary to induce a temperature change of 100°C are representative for values of Mg# between 89 and 92, which covers the range observed in this study. Unfortunately, most tomography models do not present their uncertainties. To test the effect of velocity variations, calculations were also done using the S-wave tomography SL2013sv (Schaeffer & Lebedev, 2013). Both SA2019 and SL2013sv use the same setup in terms of crustal model (CRUST2.0, Bassin et al., 2000), method ("AMI") and reference velocity. Therefore, no systematic differences of the models are expected. Instead, differences will rather be based on available data and parametrization. Results obtained are shown for the depth of 100 km (Figure 11).

In general, the temperature distributions (Figures 11a) are similar on a large scale for both tomography models. When using SL2013sv, the cratons are dominated by temperatures <1000°C and thermal densities >0.02 g/cm³ (Figures 11b), except for the Rio de la Plata Craton (mostly >1100°C and <0 g/cm³). In most areas, the temperatures from SL2013sv differ by less than 150°C from those of SA2019, inducing differences of thermal density up to 0.015 g/cm³. In addition, the compositional densities from SL2013sv in those ar-
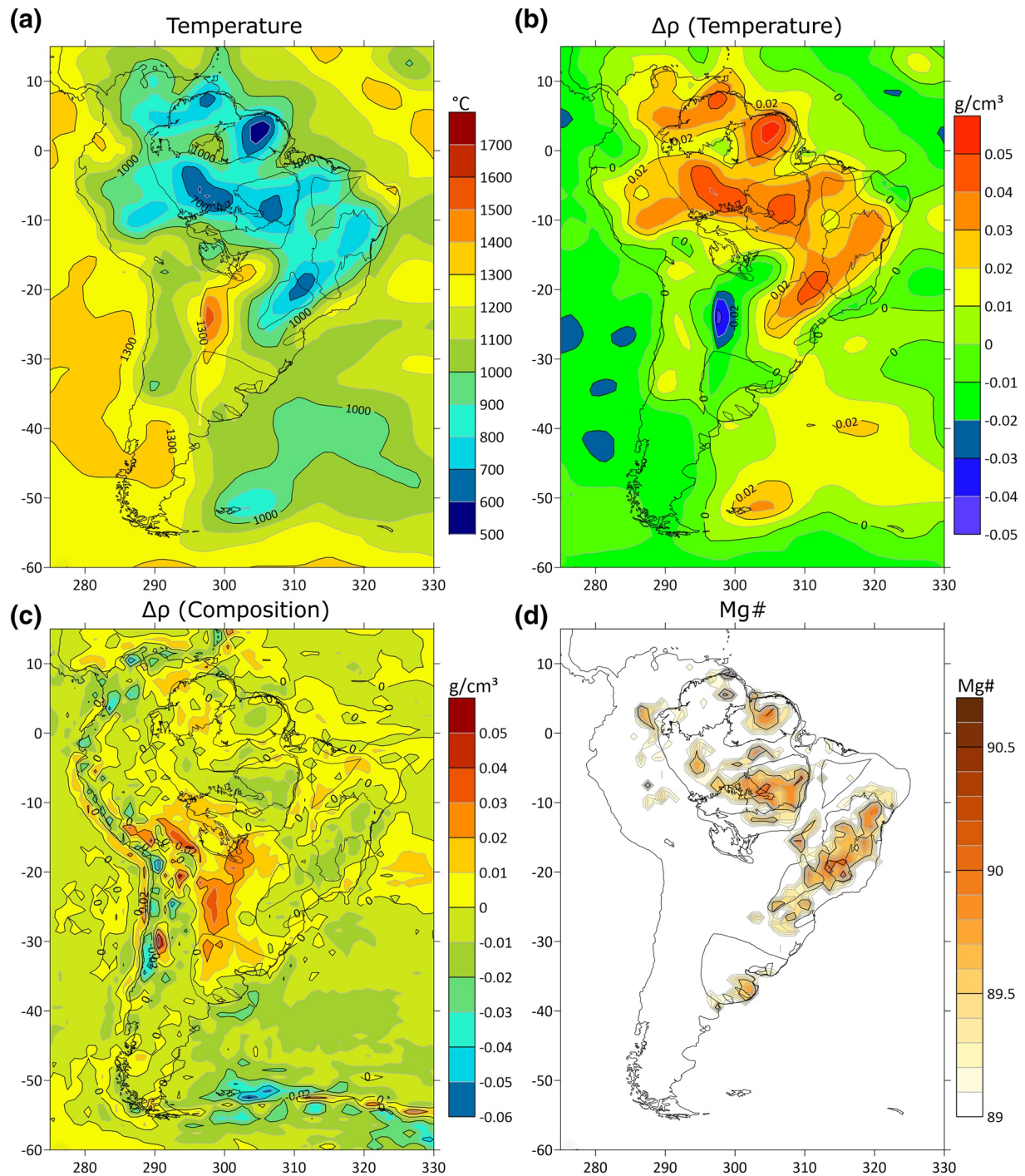
Figure 11. Results of the final iteration at a depth of 100 km based on SL2013sv: (a) Temperature, (b) Thermal density variations, (c) Compositional density variations, (d) Mg#. Colors are the same as in other results presented before for easier comparison. Temperatures tend to be lower than for SA2019. As expected, lower temperatures correlate with higher positive thermal density variations, and partially induce stronger negative compositional anomalies that cause increased values of Mg#.

eas are in the range of ±0.02 g/cm³ (Figures 11c) with differences smaller than 0.0075 g/cm³ compared to SA2019, inducing Mg# changes of at most 0.4. Temperatures as low as 600°C are found under the Solimões Basin for SL2013sv. Here, the SA2019 results are up to 250°C higher, implying stronger thermal variations up to 0.05 g/cm³. Yet the implied Mg# does not exceed 89.7 (Figures 11d) with differences <0.4 compared to

SA2019. Low temperature (i.e., high velocity) anomalies are located differently at the São Francisco Craton in SL2013sv and SA2019 (cf. Figures 11a and 9a). While low temperatures from SA2019 follow the outline of the São Francisco and Paranapanema Cratons, those from SL2013sv form an elongated, NE-SW trending feature. This leads to local temperature differences of up to 250°C and thus different locations of compositional anomalies. Although values of Mg# differ by >0.4 in those areas, the results for SL2013sv as well unambiguously denote the existence of a depleted root.

For SL2013sv, a low temperature zone <900°C appears to connect the Amazon, São Francisco and Paranapanema Cratons. It induces negative compositional density variations (minimum −0.16 g/cm³) and Mg# up 90. This feature contradicts the better resolved SA2019 and should therefore be considered as artificial. In summary, most of the temperature dependent variations are not significant, and even outliers caused by the worse resolution of SL2013sv with temperature differences up to 250°C do not challenge the presented results.

5.2. Crustal Model

Mooney and Kaban (2010) assessed the effects of uncertainties in a crustal model on the mantle gravity anomalies and residual topography for North America. It is important to note that their analysis was not related to single points of the grid but rather to broad anomalies, which are constrained by sufficient amounts of observations used for a crustal model. They showed that the uncertainty of depth to the Moho is one of the main contributors. In fact, while they estimated that 2–4 km uncertainty in depth to Moho have an effect of 30–60 mGal, they assumed a cumulative uncertainty of 35–70 mGal. This includes uncertainties of the crystalline crust and sediments, since the different sources usually do not correlate. However, corrections for the model of the crystalline crust are included in the inversion in the present study. Therefore, uncertainties of depths to the Moho constitute the main source of uncertainties implied by the crustal model. To further asses these, a density contrast across the Moho of 0.4 g/cm³ is assumed for the onshore area. This leads to uncertainties of some 30 mGal for the areas at or close to the eastern coast of Brazil. According to the interpolation uncertainties, they increase westwards reaching some 100 mGal in parts of the Andes and their forelands. The corresponding uncertainties of the residual topography range from 0.25 to 1 km for the reference density of 2.67 g/cm³. Since the uncertainty of depth to the Moho (Figure 4) presents a probably overestimated, absolute upper boundary, one can assume that the corresponding values calculated for gravity and residual topography represent an upper boundary for the total amount of uncertainties implied by the crustal model.

Two test cases were set up to check the impact on the final results. The Moho was shifted up (by subtracting the interpolation uncertainty) in the first and down (by adding the interpolation uncertainty) in the second. In either case, the input fields for the iterative approach were changed accordingly, and the calculations were repeated. When the Moho is moved upwards, it causes a positive anomaly in the crustal field, leading to smaller mantle gravity residuals after correction. At the same time, this increases crustal compensation of the topography load and thus residual topography. Considering the initial temperature model, only the gravity effect of the topmost layer is altered by changes of depth to the Moho. In result, temperatures at 100 km depth of the final model change by at most 30°C (Figure 12, top row), which results in a change of temperature related density variations by less than 0.0025 g/cm³. Therefore, most of the decreased residual mantle gravity resulting from shifting the Moho upwards is compensated by negative compositional density variations in the mantle, which lead to higher Mg# and/or extended areas of depletion (Figure 12, left and middle column). For the upwards shifted Moho, negative compositional anomalies are found in most areas of the Amazon and São Francisco Cratons. Where negative anomalies have been present in the results for the non-shifted Moho, their amplitudes are increased by less than 0.005 g/cm³. Thus, Mg# is raised by up to 0.3 in those areas. In general, compositional anomalies stay positive outside the cratons. The extent of small-scale negative compositional anomalies is increased in the areas of the Paraná Basin, proposed Rio de la Plata Craton and along the TBL. However, only those at the Paraná Basin also exist if the Moho is shifted downwards and therefore should be the only ones considered among them. The other abovementioned effects reverse if the Moho is shifted downwards by the interpolation uncertainty, respectively (Figure 12, middle and right column). In result, the areas of negative compositional anomalies and related depletion shrink toward their core areas and their amplitudes are reduced accordingly. In summary, the negative com-
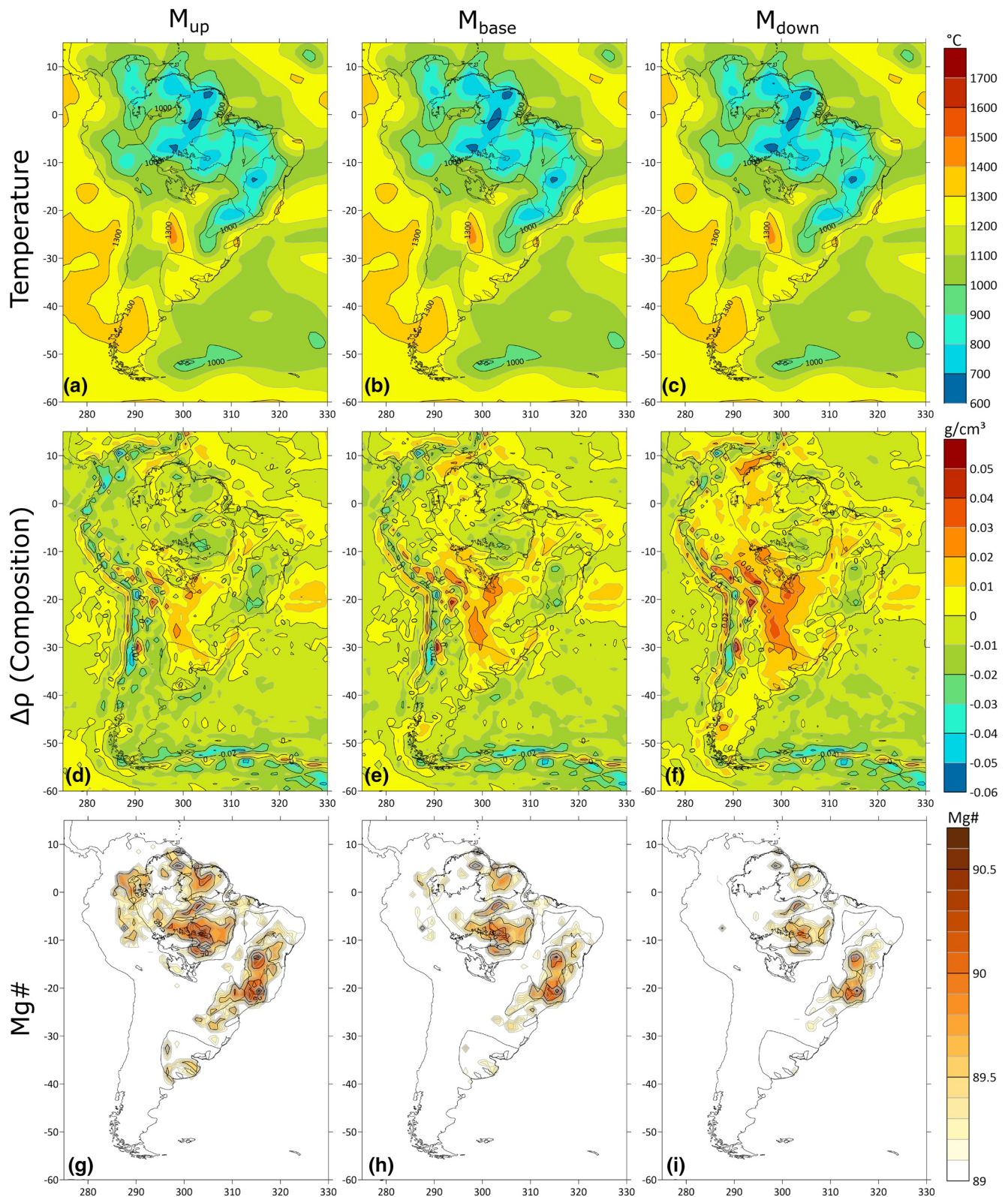
Figure 12. Results for different depths to Moho after final iteration at a depth of 100 km for temperature (top row), compositional density variations (middle row) and Mg# (bottom row). Left/right column represent an upwards/downwards shift of the Moho by the interpolation uncertainty, respectively. Colors and middle column are the same as in previous Figures for comparison. Temperature related density variations are negligible and therefore not shown.

positional anomalies persist in the Amazon, São Francisco, eastern Paranapanema Cratons and under the Paraná Basin in both cases, while the small-scale negative anomalies in the Andean forelands, the Rio de la Plata Craton and along the TBL vanish if the Moho is shifted downwards. Thus, even when overestimating the possible impact of crustal uncertainties, the iterative scheme provides stable results.

6. Discussion

6.1. Amazon Craton

Low temperatures indicate the existence of deep cratonic roots under the central Guaporé and eastern Guyana Shields (Figure 13, AA' to CC'). Their temperature minima are connected by low temperatures down to 200 km depth under the Amazon Basin (Figure 13, EE'), showing that both roots probably belong to a single, large cratonic complex. This is further supported by the negative compositional density anomalies and resulting depletion below the thick sediments of the Amazon and Solimões Basins. Celli et al. (2020) proposed an upwelling of hot mantle material under the western Guyana Shield, probably related to the Guyana Highlands and corresponding dynamic uplift. This is supported by the higher temperatures at the depths below 100 km (Figure 13, AA' and BB') and strong positive residual topography. In addition, a few negative compositional anomalies and values of Mg# > 89 exist at 100 km depth, of which only those close to the eastern part of the shield persist at all depths. They are consistent with possible errors of the Moho depth in this region (Chapter 5) and uncertainties of the tomography. Thus, probably a root existed beneath the western Guyana Shield as well, but has been widely removed by the upwelling of hot mantle material "rejuvenating" the lithospheric mantle (Figure 13, AA'). The RoSS constitutes the southernmost part of the Amazon Craton and is one of its youngest provinces (0.99–1.3 Ga, Teixeira et al., 1989). It exhibits overall higher temperatures than the rest of the Amazon Craton, partially above 1300°C at 150 km depth pointing to thin lithosphere. Since it also does not show any negative compositional densities through all depths, it probably never established a deep root. In summary, the root of the Amazon Craton was, at least in the West and South, reworked over time or never existed everywhere. Despite relatively high temperatures, depletion is imaged at the western border of the Amazon Craton, increasing westwards. The respective negative compositional anomalies (Figure 13, CC') align with the position of the subducting slab of the Nazca plate, which reaches the western Amazon region due to its flat geometry beneath Peru (Hayes et al., 2012). Therefore, the proposed depletion can be considered an artifact, caused by the cold subducting slab. To avoid such undesired imaging of the slabs, the application area of the iterative scheme was originally limited to the cratonic platform.

6.2. São Francisco and Paranapanema Cratons

The low temperatures and positive thermal density variations combined with negative compositional anomalies indicate the existence of deep depleted cratonic roots under both the São Francisco and eastern Paranapanema Cratons (Figure 13, GG'). Negative compositional anomalies and related increased Mg# demonstrate a larger subsurface extent of the São Francisco Craton than visible at the surface (Figure 9), confirming the propositions of previous works (Assumpção et al., 2017; Rocha et al., 2019). The center of low temperatures in the eastern Paranapanema Craton appears to be shifted toward the southern São Francisco Craton with increasing depth. Meanwhile, the minimum compositional anomalies and respective depletion are centered around the southern São Francisco Craton with a small secondary maximum of Mg# in the eastern Paranapanema Craton. The two cratons could not thoroughly be distinguished from each other in SA2019 (Celli et al., 2020), and the anomalies related to their roots appear amalgamated in the 1 × 1° resolution of the inversion as well (see profile HH' in the supporting information). It is also possible, that part of the root of the São Francisco Craton has been shifted westwards, comparable to what Kaban et al. (2015) showed for the root of the Superior Craton in North America. Such a shift would fit to the westward direction of mantle flow in the area (Hu et al., 2017) and the distribution of compositional anomalies and Mg# in profile GG' (Figure 13). However, this cannot be finally concluded from the results and needs further investigation. Eventually, additional data and further improvement of seismic inversion techniques (e.g., Yuan et al., 2020) and their application (e.g., Ciardelli et al., 2019) will allow to increase regional resolution and solve this puzzle in the future. The picture is further complicated by the Paraná Flood Basalts that cover the Paranapanema Craton and surrounding areas mostly south of it. Here, minor depletion is imaged down
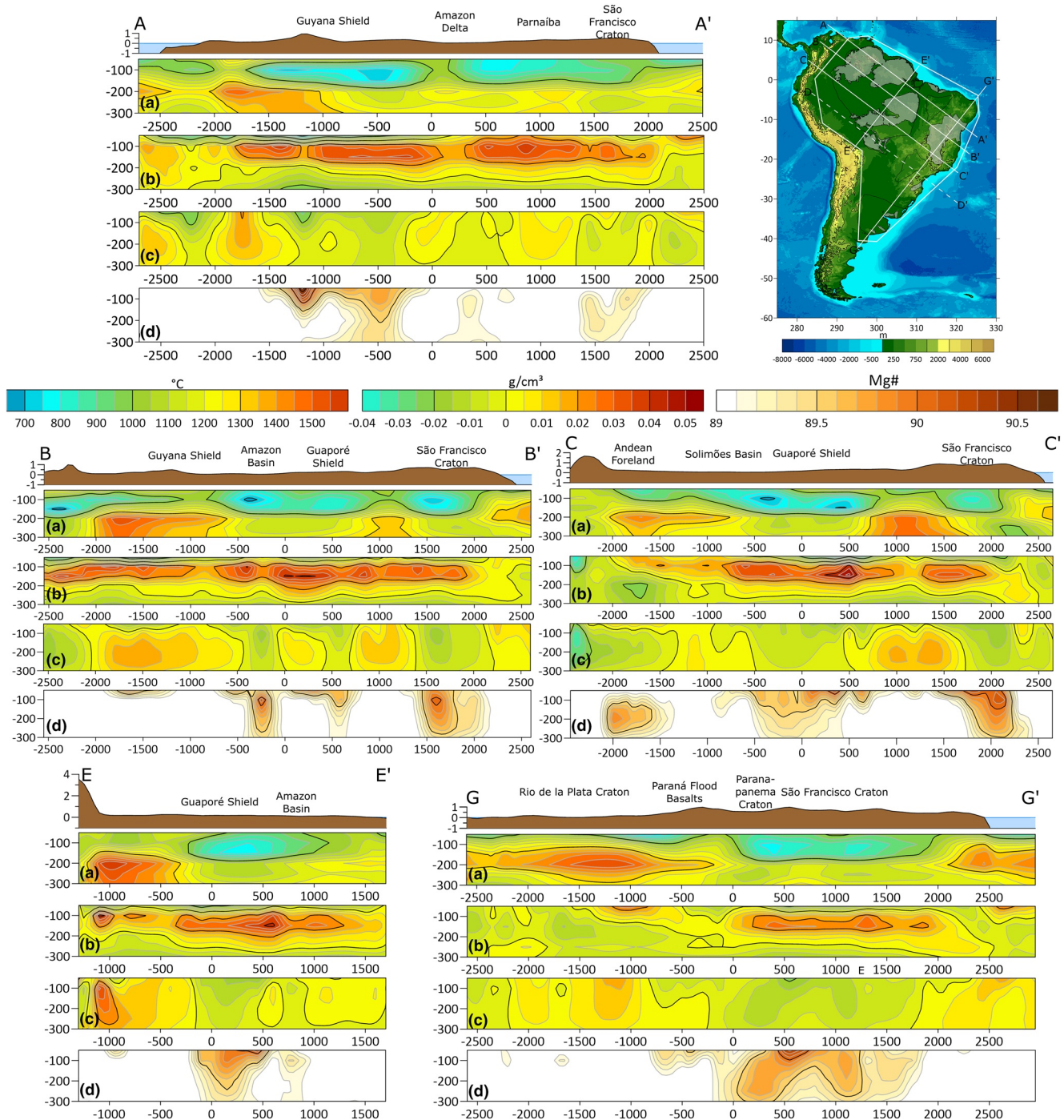
Figure 13. Five vertical profiles through the study area, each showing (a) temperature, (b) total density variation (i.e., sum of thermal and compositional variations), (c) compositional variations, and (d) Mg#. Locations are shown on the topography map in the upper right. For AA' through CC', profile km 0 is at the intersection with EE'. For EE' and GG', km 0 is at the intersection with CC' and DD', respectively. Color ranges match those of previous figures, with halved contour intervals for temperature and density to improve visibility of gradients.

to a depth of 150 km (Figure 13, GG'). This indicates that the Paranapanema Craton once exhibited a much wider extent than proposed by Mantovani et al. (2005) and that its root was largely rejuvenated prior, or synchronous, to emplacement of the flood basalts. This is supported by the results of Chaves et al. (2016), who found P-wave velocity structures typical for cratons, but along with increased densities, which they attributed to refertilization caused by uprising asthenospheric components. Such a scenario could also explain high

conductivities in the area (Bologna et al., 2019). Alternatively, parts of the observed depletion could be due to partial melting and subsequent melt removal by the upwelling of hot mantle material. In both cases, the source of the flood basalts strongly influenced the lithospheric composition.

6.3. Luiz Alves and São Luis

In general, depletion is reduced or inexistent along the coastal areas of the South American cratons. This also holds true for the cratonic fragments São Luis in northern Brazil, which was part of the Westafrican Craton before breakup, and Luiz Alves south of the Paranapanema Craton. None of the two shows distinct anomalies related to their extent (Figure 9). If they ever developed cratonic roots, they are probably too small to be represented in the tomography model or the inversion. Moreover, due to their proximity to the coast, those blocks probably have been significantly affected by metasomatic processes during the Atlantic opening, which could have refertilized previously existent roots.

6.4. Rio de la Plata Craton

Oyhantçabal et al. (2011) found evidence of cratonic crust in boreholes in the Andean Forelands and thus proposed a wide extend of the Rio de la Plata Craton, reaching from the coastal areas of northern Argentina to the forelands. In contrast, depletion found in this study is mostly limited to the craton's outcrops close to the coast at a depth of 100 km and not fully confirmed by the uncertainty assessment (Chapter 5). In addition, temperatures exceed 1300°C at 150 km depth, indicating a thin lithosphere (Figure 13, GG'). Moreover, resolution tests by Celli et al. (2020) showed that their tomography would have discovered a deep, widespread cratonic root. An even larger extent towards the North was proposed by Santos et al. (2019), including the Paranapanema and almost bordering the São Francisco Craton. This is opposed by low temperatures and depletion (Mg# up to 89.8) in the Paranapanema Craton. Moreover, a separation of the two cratons is corroborated by the Western Parana suture zone (Dragone et al., 2017), and results from magnetotelluric studies (Bologna et al., 2019). In summary, if a cratonic root ever existed, it is almost completely reworked by now and probably never extended that far. In a different scenario, the cratonic crust found by Oyhantcabal et al. (2011) near the Andes could belong to a different cratonic fragment that never developed a deep root and not to the Rio de la Plata Craton.

6.5. Parnaíba Basin

The Parnaíba Basin in northeastern Brazil is marked by low temperatures (<1000°C) down to a depth of 150 km that appear to concatenate those in the eastern Amazon and western São Francisco Cratons (Figure 13, AA'). Celli et al. (2020) argue for the existence of a cratonic root based on fast seismic velocities under the northern part of the basin. They attribute the apparent connection with the two neighboring cratons to the fact that the corridors separating the basin from them might be too narrow to be resolved by their model. The separation becomes evident from positive compositional densities at the Parnaíba Basin, which are flanked by negative ones of the neighboring cratons (Figure 13, AA'). De Castro et al. (2014) argue for three areas of cratonic basement under the Parnaíba Basin based on potential field data. Tozer et al. (2017) confirm the existence of a high density body in the lower crust that might extend into the upper mantle, but favor a magmatic origin. However, the temperatures <1300°C found in the presented results down to a depth of 200 km indicate thick lithosphere, yet the positive compositional anomalies do not support the existence of a deep depleted cratonic root.

7. Conclusions

We present a new, three-dimensional, self-consistent model of temperature, density, and compositional variations of the South American upper mantle from the Moho to a depth of 325 km. Seismic tomography, data on the crustal structure and gravity field were combined with mineral physics constraints in an iterative inversion scheme.

The average crystalline crust density ranges from 2.825 to 2.9 g/cm³ for most of the stable platform with high densities (2.9–2.925 g/cm³) in the area of the Paraná Flood Basalts. Densities observed for the Andean

Forelands are higher than for the platform, ranging from 2.875 to 2.925 g/cm³. As expected, the lowest crustal densities occur in the Andes, where they are smaller than 2.825 g/cm³, in general.

The iterative scheme yields deep, depleted lithospheric roots under significant parts of the Amazon, São Francisco and Paranapanema Cratons denoted by temperatures and Mg# ranging from almost 800°C and up to 90.7 at 100 km to almost 1200°C and Mg# > 89.5 at 200 km depth, respectively.

At the northwestern Amazon Craton, temperatures up to some 1200°C at 150 km depth and above 1400°C at 200 km depth indicate that the cratonic root was removed, possibly by upwelling of hot mantle material. Almost no negative compositional anomalies were found at the São Luis, Parnaíba, Luiz Alves and Rio de la Plata Cratons. Temperatures at the first two cratons are below 1300°C at 200 km depth, indicating a thick lithosphere, while the other two cratons show high temperatures (>1200°C at 100 and >1400°C at the depth of 150 km), indicating the absence of deep cratonic roots. The small negative compositional anomalies and depletion at 100 km of depth in the coastal areas of the Rio de la Plata Craton point to former existence of a depleted root, but the proposed wide extension is not confirmed.

The anomalies under the São Francisco and Paranapanema Cratons appear concatenated. This could be caused by a shifted root of the São Francisco Craton toward the Paranapanema, but it is also possible that this is caused by insufficient resolution of the employed seismic tomography. However, the anomalies denote a wider extent of the São Francisco Craton than its outcropping part. Further to the South, depletion is indicated by negative compositional anomalies up to the depth of 150 km in the area of the Paraná Flood Basalts. These anomalies probably are the remnants of a previously larger extent of the Paranapanema Craton and were reworked by the upwelling of hot mantle material that lead to emplacement of the Flood Basalts, demonstrating a strong influence on the lithospheric structure.

The final inversion results were tested with respect to the most significant uncertainty sources, which are related to the employed depth to the Moho and seismic tomography. The tests show that, while these uncertainties have quantitative effects to be considered in the interpretation, they do not qualitatively challenge the main results.

Data Availability Statement

Data of the models described here are published via GFZ Data Services: https://doi.org/10.5880/GFZ.1.3.2020.006 (Finger et al., 2020). Data from the GSC used to compile the crustal and sediment density models are available from Walter Mooney (mooney@usgs.gov) upon request.

References

Amante, C., & Eakins, B. W. (2009). ETOPO1 1 Arc-Minute Global Relief Model: Procedures, data sources and analysis. *NOAA Technical Memorandum NESDIS NGDC-24.* https://doi.org/10.7289/V5C8276M

Araujo, S. (2013). The Ecuadorian moho. *La Granja*, *18*(2), 43. https://doi.org/10.17163/lgr.n18.2013.03

Assumpção, M., Azevedo, P. A., Rocha, M. P., & Bianchi, M. B. (2017). Lithospheric features of the São Francisco craton. In M. Heilbron, U. G. Cordani, & F. Alkmim (Eds.), *São Francisco Craton, Eastern Brazil* (pp. 15–25). Cham: Springer. https://doi.org/10.1007/978-3-319-01715-0_2

Assumpção, M., Feng, M., Tassara, A., & Julià, J. (2013). Models of crustal thickness for South America from seismic refraction, receiver functions and surface wave tomography. *Tectonophysics*, *609*, 82–96. https://doi.org/10.1016/j.tecto.2012.11.014

Bassin, C., Laske, G., & Masters, G. (2000). The current limits of resolution for surface wave tomography in North America. *EOS Transactions AGU*, *81*, F897. Retrieved from https://igppweb.ucsd.edu/~gabi/crust2.html

Bologna, M. S., Dragone, G. N., Muzio, R., Peel, E., Nuñez-Demarco, P., & Ussami, N. (2019). Electrical structure of the lithosphere from Rio de la Plata Craton to Paraná Basin: Amalgamation of Cratonic and Refertilized Lithospheres in SW Gondwanaland. *Tectonics*, *38*(1), 77–94. https://doi.org/10.1029/2018TC005148

Brocher, T. M. (2005). Empirical relations between elastic wavespeeds and density in the Earth's crust. *Bulletin of the Seismological Society of America*, *95*(6), 2081–2092. https://doi.org/10.1785/0120050077

Cammarano, F., Goes, S., Vacher, P., & Giardini, D. (2003). Inferring upper-mantle temperatures from seismic velocities. *Physics of the Earth and Planetary Interiors*, *138*(3–4), 197–222. https://doi.org/10.1016/S0031-9201(03)00156-0

Celli, N. L., Lebedev, S., Schaeffer, A. J., Ravenna, M., & Gaina, C. (2020). The upper mantle beneath the South Atlantic Ocean, South America and Africa from waveform tomography with massive data sets. *Geophysical Journal International*, *221*(1), 178–204. https://doi.org/10.1093/gji/ggz574

Chaves, C., Ussami, N., & Ritsema, J. (2016). Density and P-wave velocity structure beneath the Paraná Magmatic Province: Refertilization of an ancient lithospheric mantle. *Geochemistry, Geophysics, Geosystems*, *17*(8), 3054–3074. https://doi.org/10.1002/2016GC006369

Christensen, N. I., & Mooney, W. D. (1995). Seismic velocity structure and composition of the continental crust: A global view. *Journal of Geophysical Research*, *100*(B6), 9761–9788. https://doi.org/10.1029/95JB00259

Chulick, G. S., Detweiler, S., & Mooney, W. D. (2013). Seismic structure of the crust and uppermost mantle of South America and surrounding oceanic basins. *Journal of South American Earth Sciences*, *42*, 260–276. https://doi.org/10.1016/j.jsames.2012.06.002

Ciardelli, C., Van der Lee, S., Bozdag, E., Assumpção, M., Ciardelli, C., Van der Lee, S., et al. (2019). Adjoint tomography of South America based on 3D spectral-element seismic wave simulations. In *AGU Fall Meeting Abstracts*. AGU. Retrieved from https://ui.adsabs.harvard.edu/abs/2019AGUFM.T21F0380C/abstract

Cordani, U. G., Ramos, V. A., Fraga, L. M., Cegarra, M., Delgado, I., Souza, K. G. D., et al. (2016). *Tectonic map of South America=Mapa tectônico da América do Sul* (2nd ed.). Paris: CGMW-CPRM-SEGEMAR. Retrieved from http://rigeo.cprm.gov.br/jspui/handle/doc/16750

Cordani, U. G., Sato, K., Teixeira, W., Tassinari, C. C. G., & Basei, M. A. S. (2000). Crustal evolution of the South American platform. In U. G. Cordani, E. J. Milani, A. Thomaz Filho & D. A. Campos (Eds.), *Tectonic evolution of South America* (pp. 19–40). Rio de Janeiro: 31st International Geological Congress.

de Brito Neves, B. B., & Cordani, U. G. (1991). Tectonic evolution of South America during the Late Proterozoic. *Precambrian Research*, *53*(1–2), 23–40. https://doi.org/10.1016/0301-9268(91)90004-T

de Brito Neves, B. B., & Fuck, R. A. (2013). Neoproterozoic evolution of the basement of the South-American platform. *Journal of South American Earth Sciences*, *47*, 72–89. https://doi.org/10.1016/j.jsames.2013.04.005

de Castro, D. L., Bezerra, F. H., Fuck, R. A., & Vidotti, R. M. (2016). Geophysical evidence of pre-sag rifting and post-rifting fault reactivation in the Parnaíba basin, Brazil. *Solid Earth*, *7*(2), 529–548. https://doi.org/10.5194/se-7-529-2016

de Castro, D. L., Fuck, R. A., Phillips, J. D., Vidotti, R. M., Bezerra, F. H. R., & Dantas, E. L. (2014). Crustal structure beneath the Paleozoic Parnaíba Basin revealed by airborne gravity and magnetic data, Brazil. *Tectonophysics*, *614*, 128–145. https://doi.org/10.1016/j.tecto.2013.12.009

Dragone, G. N., Ussami, N., Gimenez, M. E., Lince Klinger, F. G., & Chaves, C. A. M. (2017). Western Paraná suture/shear zone and the limits of Rio Apa, Rio Tebicuary and Rio de la Plata cratons from gravity data. *Precambrian Research*, *291*, 162–177. https://doi.org/10.1016/j.precamres.2017.01.029

Dziewonski, A. M., & Anderson, D. L. (1981). Preliminary reference Earth model. *Physics of the Earth and Planetary Interiors*, *25*(4), 297–356. https://doi.org/10.1016/0031-9201(81)90046-7

Exxon Production Research Company. (1985). *Tectonic map of the world 1: 10 000 000*. Houston: Exxon Production Research Company.

Finger, N.-P., Kaban, M. K., Tesauro, M., Haeger, C., Mooney, W. D., & Thomas, M. (2020). *A thermo-compositional model of the Cratonic lithosphere of South America: Models of the upper mantle, crust and sediment density*. Potsdam: GFZ Data Services. https://doi.org/10.5880/GFZ.1.3.2020.006

Font, Y., Segovia, M., Vaca, S., & Theunissen, T. (2013). Seismicity patterns along the ecuadorian subduction zone: New constraints from earthquake location in a 3-D a priori velocity model. *Geophysical Journal International*, *193*(1), 263–286. https://doi.org/10.1093/gji/ggs083

Förste, C., Bruinsma, S., Abrikosov, O., Flechtner, F., Marty, J.-C., Lemoine, J.-M., et al. (2014). *EIGEN-6C4-The latest combined global gravity field model including GOCE data up to degree and order 1949 of GFZ Potsdam and GRGS Toulouse*. Potsdam: GFZ Data Services. https://doi.org/10.5880/icgem.2015.1

Gardner, G. H. F., Gardner, L. W., & Gregory, A. R. (1974). Formation velocity and density-the diagnostic basics for stratigraphic traps. *Geophysics*, *39*(6), 770–780. Retrieved from https://pubs.geoscienceworld.org/geophysics/article-pdf/39/6/770/3156615/770.pdf

Griffin, W. L., O'Reilly, S. Y., Abe, N., Aulbach, S., Davies, R. M., Pearson, N. J., et al. (2003). The origin and evolution of Archean lithospheric mantle. *Precambrian Research*, *127*, 19–41. https://doi.org/10.1016/S0301-9268(03)00180-3

Haas, P., Ebbing, J., & Szwillus, W. (2020). Sensitivity analysis of gravity gradient inversion of the Moho depth-a case example for the Amazonian Craton. *Geophysical Journal International*, *221*, 1896–1912. https://doi.org/10.1093/gji/ggaa122

Haeger, C., Kaban, M. K., Tesauro, M., Petrunin, A. G., & Mooney, W. D. (2019). 3-D density, thermal, and compositional model of the Antarctic Lithosphere and Implications for Its Evolution. *Geochemistry, Geophysics, Geosystems*, *20*(2), 688–707. https://doi.org/10.1029/2018GC008033

Hayes, G. P., Wald, D. J., & Johnson, R. L. (2012). Slab1.0: A three-dimensional model of global subduction zone geometries. *Journal of Geophysical Research*, *117*(B01302). https://doi.org/10.1029/2011JB008524

Heintz, M., Debayle, E., & Vauchez, A. (2005). Upper mantle structure of the South American continent and neighboring oceans from surface wave tomography. *Tectonophysics*, *406*(1–2), 115–139. https://doi.org/10.1016/j.tecto.2005.05.006

Hirth, G., Evans, R. L., & Chave, A. D. (2000). Comparison of continental and oceanic mantle electrical conductivity: Is the Archean lithosphere dry? *Geochemistry, Geophysics, Geosystems*, *1*(12), 1030. https://doi.org/10.1029/2000GC000048

Hu, J., Faccenda, M., & Liu, L. (2017). Subduction-controlled mantle flow and seismic anisotropy in South America. *Earth and Planetary Science Letters*, *470*, 13–24. https://doi.org/10.1016/j.epsl.2017.04.027

Jackson, I., Fitz Gerald, J. D., Faul, U. H., & Tan, B. H. (2002). Grain-size-sensitive seismic wave attenuation in polycrystalline olivine. *Journal of Geophysical Research*, *107*(B12), ECV51–ECV516. https://doi.org/10.1029/2001jb001225

Jordan, T. H. (1978). Composition and development of the continental tectosphere. *Nature*, *274*(5671), 544–548. https://doi.org/10.1038/274544a0

Kaban, M. K., El Khrepy, S., & Al-Arifi, N. (2016). Isostatic model and isostatic gravity anomalies of the Arabian plate and surroundings. *Pure and Applied Geophysics*, *173*(4), 1211–1221. https://doi.org/10.1007/s00024-015-1164-0

Kaban, M. K., & Mooney, W. D. (2001). Density structure of the lithosphere in the southwestern United States and its tectonic significance. *Journal of Geophysical Research*, *106*(B1), 721–739. https://doi.org/10.1029/2000JB900235

Kaban, M. K., Mooney, W. D., & Petrunin, A. G. (2015). Cratonic root beneath North America shifted by basal drag from the convecting mantle. *Nature Geoscience*, *8*(10), 797–800. https://doi.org/10.1038/ngeo2525

Kaban, M. K., Schwintzer, P., Artemieva, I. M., & Mooney, W. D. (2003). Density of the continental roots: Compositional and thermal contributions. *Earth and Planetary Science Letters*, *209*(1–2), 53–69. https://doi.org/10.1016/S0012-821X(03)00072-4

Kaban, M. K., Stolk, W., Tesauro, M., El Khrepy, S., Al-Arifi, N., Beekman, F., et al. (2016). 3D density model of the upper mantle of Asia based on inversion of gravity and seismic tomography data. *Geochemistry, Geophysics, Geosystems*, *17*(11), 4457–4477. https://doi.org/10.1002/2016GC006458

Kaban, M. K., Tesauro, M., & Cloetingh, S. (2010). An integrated gravity model for Europe's crust and upper mantle. *Earth and Planetary Science Letters*, *296*(3–4), 195–209. https://doi.org/10.1016/j.epsl.2010.04.041

Kaban, M. K., Tesauro, M., Mooney, W. D., & Cloetingh, S. A. P. L. (2014). Density, temperature, and composition of the North American lithosphere-new insights from a joint analysis of seismic, gravity, and mineral physics data: 1. Density structure of the crust and upper mantle. *Geochemistry, Geophysics, Geosystems*, *15*(12), 4781–4807. https://doi.org/10.1002/2014GC005483

Laske, G., Masters, G., Ma, Z., & Pasyanos, M. (2013). Update on CRUST1.0—A 1-degree global model of Earth's crust. In *EGU General Assembly* (Vol. 15, p. 2658). Vienna: EGU. Retrieved from https://ui.adsabs.harvard.edu/abs/2013EGUGA.15.2658L/abstract

Lee, C.-T. A. (2003). Compositional variation of density and seismic velocities in natural peridotites at STP conditions: Implications for seismic imaging of compositional heterogeneities in the upper mantle. *Journal of Geophysical Research*, *108*(B9), 2441. https://doi.org/10.1029/2003jb002413

Ludwig, W. J., Nafe, J. E., & Drake, C. L. (1970). Seismic refraction. In A. E. Maxwell (Ed.), The sea (Vol. 4, pp. 53–84). New York, NY: Wiley-Interscience.

Mantovani, M. S. M., Quintas, M. C. L., Shukowsky, W., & de Brito Neves, B. B. (2005). Delimitation of the Paranapanema proterozoic block: A geophysical contribution. *Episodes*, *28*(1), 18–22. https://doi.org/10.18814/epiiugs/2005/v28i1/002

McDonough, W. F., & Sun, S. S. (1995). The composition of the Earth. *Chemical Geology*, *120*(3–4), 223–253. https://doi.org/10.1016/0009-2541(94)00140-4

Milani, E. J., & Thomaz Filho, A. (2000). Sedimentary Basins of the South America. In E. J. Milani, A. Thomaz Filho, & D. A. Campos (Eds.), *Umberto Giuseppe Cordani Tectonic evolution of South America* (pp. 389–449). Rio de Janeiro: 31st International Geological Congress.

Mooney, W. D. (2015). Crust and lithospheric structure – Global crustal structure. In G. Schubert, B. Romanowicz, & A. Dziewonski (Eds.), *Treatise on geophysics* (2nd ed., pp. 339–390). Elsevier.

Mooney, W. D., & Kaban, M. K. (2010). The North American upper mantle: Density, composition, and evolution. *Journal of Geophysical Research*, *115*(B12), B12424. https://doi.org/10.1029/2010JB000866

Mooney, W. D., Meyer, R. P., Laurence, J. P., Meyer, H., & Ramfrez, A. J. E. (1979). Seismic refraction studies of the western Cordillera, Colombia. *Bulletin of the Seismological Society of America*, *69*, 1745–1761. Retrieved from https://pubs.geoscienceworld.org/ssa/bssa/article-pdf/69/6/1745/2702532/BSSA0690061745.pdf

Murphy, B., Müller, S., & Yurchak, R. (2020). *GeoStat-framework/PyKrige: v1.5.0*. https://doi.org/10.5281/ZENODO.3739879

Novella, D., Bolfan-Casanova, N., Nestola, F., & Harris, J. W. (2015). H$_2$O in olivine and garnet inclusions still trapped in diamonds from the Siberian craton: Implications for the water content of cratonic lithosphere peridotites. *Lithos*, *230*, 180–183. https://doi.org/10.1016/j.lithos.2015.05.013

Nunn, J. A., & Aires, J. R. (1988). Gravity anomalies and flexure of the lithosphere at the Middle Amazon Basin, Brazil. *Journal of Geophysical Research*, *93*(B1), 415–428. https://doi.org/10.1029/JB093iB01p00415

Oyhantçabal, P., Siegesmund, S., & Wemmer, K. (2011). The Río de la Plata Craton: A review of units, boundaries, ages and isotopic signature. *International Journal of Earth Sciences*, *100*(2), 201–220. https://doi.org/10.1007/s00531-010-0580-8

Pankhurst, R. J., Rapela, C. W., Fanning, C. M., & Márquez, M. (2006). Gondwanide continental collision and the origin of Patagonia. *Earth-Science Reviews*, *76*(3–4), 235–257. https://doi.org/10.1016/j.earscirev.2006.02.001

Ritsema, J., Deuss, A., van Heijst, H. J., & Woodhouse, J. H. (2011). S40RTS: A degree-40 shear-velocity model for the mantle from new Rayleigh wave dispersion, teleseismic traveltime and normal-mode splitting function measurements. *Geophysical Journal International*, *184*(3), 1223–1236. https://doi.org/10.1111/j.1365-246X.2010.04884.x

Rivadeneyra-Vera, C., Bianchi, M., Assumpção, M., Cedraz, V., Julià, J., Rodríguez, M., et al. (2019). An updated crustal thickness map of central South America based on receiver function measurements in the region of the Chaco, Pantanal, and Paraná Basins, Southwestern Brazil. *Journal of Geophysical Research: Solid Earth*, *124*(8), 1–15. https://doi.org/10.1029/2018jb016811

Rizzotto, G. J., & Hartmann, L. A. (2012). Geological and geochemical evolution of the Trincheira Complex, a Mesoproterozoic ophiolite in the southwestern Amazon craton, Brazil. *Lithos*, *148*, 277–295. https://doi.org/10.1016/j.lithos.2012.05.027

Rocha, M. P., de Azevedo, P. A., Assumpção, M., Pedrosa-Soares, A. C., Fuck, R., & Von Huelsen, M. G. (2019). Delimiting the Neoproterozoic São Francisco Paleocontinental Block with P-wave traveltime tomography. *Geophysical Journal International*, *219*(1), 633–644. https://doi.org/10.1093/gji/ggz323

Sanchez Bettucci, L., Peel, E., & Oyhantçabal, P. (2010). Precambrian geotectonic units of the Rio de la Plata craton. *International Geology Review*, *52*(1), 32–50. https://doi.org/10.1080/00206810903211104

Santos, J. O. S., Chernicoff, C. J., Zappettini, E. O., McNaughton, N. J., & Hartmann, L. A. (2019). Large geographic and temporal extensions of the Río de la Plata Craton, South America, and its metacratonic eastern margin. *International Geology Review*, *61*(1), 56–85. https://doi.org/10.1080/00206814.2017.1405747

Schaeffer, A. J., & Lebedev, S. (2013). Global shear speed structure of the upper mantle and transition zone. *Geophysical Journal International*, *194*(1), 417–449. https://doi.org/10.1093/gji/ggt095

Schaeffer, A. J., & Lebedev, S. (2015). Global heterogeneity of the lithosphere and underlying mantle: A seismological appraisal based on multimode surface-wave dispersion analysis, shear-velocity tomography, and tectonic regionalization. In A. Khan & F. Deschamps (Eds.), *The earth's heterogeneous mantle: A geophysical, geodynamical, and geochemical perspective* (pp. 3-46). Cham: Springer International Publishing. https://doi.org/10.1007/978-3-319-15627-9_1

Silva, J. B., Costa, D. C., & Barbosa, V. C. (2006). Gravity inversion of basement relief and estimation of density contrast variation with depth. *Geophysics*, *71*(5), J51–J58. https://doi.org/10.1190/1.2236383

Steinberger, B., & Becker, T. W. (2018). A comparison of lithospheric thickness models. *Tectonophysics*, *746*, 325–338. https://doi.org/10.1016/j.tecto.2016.08.001

Stixrude, L., & Lithgow-Bertelloni, C. (2005). Thermodynamics of mantle minerals – I. Physical properties. *Geophysical Journal International*, *162*, 610–632. https://doi.org/10.1111/j.1365-246X.2005.02642.x

Stolk, W., Kaban, M. K., Beekman, F., Tesauro, M., Mooney, W. D., & Cloetingh, S. (2013). High resolution regional crustal models from irregularly distributed data: Application to Asia and adjacent areas. *Tectonophysics*, *602*, 55–68. https://doi.org/10.1016/j.tecto.2013.01.022

Tassara, A., & Echaurren, A. (2012). Anatomy of the Andean subduction zone: Three-dimensional density model upgraded and compared against global-scale models. *Geophysical Journal International*, *189*(1), 161–168. https://doi.org/10.1111/j.1365-246X.2012.05397.x

Teixeira, W., Tassinari, C., Cordani, U. G., & Kawashita, K. (1989). A review of the geochronology of the Amazonian Craton: Tectonic implications. *Precambrian Research*, *42*(3–4), 213–227. https://doi.org/10.1016/0301-9268(89)90012-0

Tesauro, M., Kaban, M. K., Mooney, W. D., & Cloetingh, S. A. P. L. (2014a). Density, temperature, and composition of the North American lithosphere – New insights from a joint analysis of seismic, gravity, and mineral physics data: 2. Thermal and compositional model of the upper mantle. *Geochemistry, Geophysics, Geosystems*, *15*(12), 4808–4830. https://doi.org/10.1002/2014GC005484

Tesauro, M., Kaban, M. K., Mooney, W. D., & Cloetingh, S. (2014b). NACr14: A 3D model for the crustal structure of the North American Continent. *Tectonophysics*, *631*, 65–86. https://doi.org/10.1016/j.tecto.2014.04.016

Tozer, B., Watts, A. B., & Daly, M. C. (2017). Crustal structure, gravity anomalies, and subsidence history of the Parnaíba cratonic basin, Northeast Brazil. *Journal of Geophysical Research: Solid Earth*, *122*(7), 5591–5621. https://doi.org/10.1002/2017JB014348

Uieda, L., & Barbosa, V. C. F. (2017). Fast nonlinear gravity inversion in spherical coordinates with application to the South American Moho. *Geophysical Journal International*, *208*(1), 162–176. https://doi.org/10.1093/gji/ggw390

van der Meijde, M., Julià, J., & Assumpção, M. (2013). Gravity derived Moho for South America. *Tectonophysics*, *609*, 456–467. https://doi.org/10.1016/j.tecto.2013.03.023

Yuan, Y. O., Bozdağ, E., Ciardelli, C., Gao, F., & Simons, F. J. (2020). The exponentiated phase measurement, and objective-function hybridization for adjoint waveform tomography. *Geophysical Journal International*, *221*(2), 1145–1164. https://doi.org/10.1093/gji/ggaa063